Submitted to J. Crystal Growth

NASA
HOLD PENDING RB
6.9.83

RADIAL SEGREGATION INDUCED BY NATURAL CONVECTION AND MELT/SOLID INTERFACE SHAPE IN VERTICAL BRIDGMAN GROWTH

by

Chiechun J. Chang[†] and Robert A. Brown[*]

Department of Chemical Engineering and
Materials Processing Center
Massachusetts Institute of Technology
Cambridge, MA 02139

November 1982

Abstract

The roles of natural convection in the melt and the shape of the melt/solid interface on radial dopant segregation are analyzed for a prototype of vertical Bridgman crystal growth system by finite element methods that solve simultaneously for the velocity field in the melt, the shape of the solidification isotherm, and the temperature distribution in both phases. Results are presented for crystal and melt with thermophysical properties similar to those of gallium-doped germanium in Bridgman configurations with melt below (thermally destabilizing) and above (stabilizing) the crystal. Steady axisymmetric flows are classified according to Rayleigh number as either being nearly the growth velocity, having a weak cellular structure or having large amplitude cellular convection. The flows in the two Bridgman configurations are driven by different temperature gradients and are in opposite directions. Finite element calculations for the transport of a dilute dopant by these flow fields reveal radial segregation levels as large as sixty percent of the mean concentration. Segregation is found most severe at an intermediate value of Rayleigh number above which the dopant distribution along the interface levels as the intensity of the flow increases. The complexity of the concentration field coupled with calculations of effective segregation coefficient show the coarseness of the usual diffusion-layer approximation for describing the dopant distribution adjacent to the crystal. The length of the gradient zone and the ratio of thermal conductivities between melt and crystal are identified as additional critical parameters for setting the degree of radial segregation. The predictions of melt/solid interface shape and axial and radial dopant segregation will form the basis for the first comparison between detailed fluid mechanical models of melt crystal growth and actual experiments.

---

[*] Correspondence should be directed to R.A. Brown.

[†] Present address: Texas Instruments Corporation, Dallas, Texas.

(NASA-CR-173627) RADIAL SEGREGATION INDUCED BY NATURAL CONVECTION AND MELT/SOLID INTERFACE SHAPE IN VERTICAL BRIDGMAN GROWTH (Massachusetts Inst. of Tech.) 66 p HC A04/MF A01 CSCL 20B G3/76

N84-27571

Unclas
13637

1. INTRODUCTION

The compositional uniformity of dopants and impurities in semiconductor crystals grown from the melt depends strongly on the pattern and intensity of flow in the melt and on the shape of the melt/solid interface. In processes such as the Czochralski and floating zone methods for producing silicon and the vertical Bridgman configuration studied here, the unequal partitioning of dopant between melt and crystal during solidification causes a concentration gradient perpendicular to the melt/solid interface. When the melt/solid interface is planar and the melt is quiescent except for motion caused by crystal growth the concentration field decays exponentially with distance into the melt. Curvature of the solidification interface and convection in the melt both change the concentration distribution along the interface and alter the dopant level in the crystal.

The effect of convection on segregation in the growth direction was pointed out by the Burton _et al._ analysis [1-2] of the effect of crystal rotation on mass transfer. When the crystal diameter is large and the velocity field is similar along the radius of the melt/solid interface convection only alters the concentration field perpendicular to the interface. Burtin _et al._ analyzed this case and developed an expression for an effective segregation coefficient and introduced the notion of an axial "boundary layer" thickness for diffusion controlled mass transfer. Others [4-8] have applied the idea of a uniform diffusion-layer or stagnant-film that is masking a growing crystal from a well mixed bulk and have determined so-called boundary-layer (more appropriately called diffusion-layer) thicknesses without any picture for the fluid motion in the melt. Other than Burtin, Prim and Slichter's original analysis of rotating flows, few papers dealing with melt crystal growth [9-10] have addressed the exact coupling between the fluid flow and mass transfer in a consistent way.

In many growth configurations, the concept of a uniform diffusion-layer yields an over-simplified view of the role of convection in dopant segregation [11]. When the flow is laminar and cellular, as is the case for many small-scale growth systems and for reduced gravity experiments, convective mass transfer is uneven along the surface of the crystal and significant radial segregation results. The coupling between moderate convection and radial dopant segregation has been thoroughly analyzed for the rotationally-driven flows in small-scale floating zones [10, 12, 13] and has been demonstrated for buoyancy-driven convection under microgravity conditions [14]. All these studies were of model crystal growth systems with planar solidification interfaces.

Coriell and Sekerka ([15]; also see ref. 16) have demonstrated that significant radial segregation occurs in systems without convection tangent to the crystal surface when the radius of curvature of this interface is the same or less than the length scale of the concentration gradient adjacent to the interface. Curvature-induced segregation has been shown to be an important contribution to dopant inhomogeneities in capillary growth systems [17-19] and may be important in other small-scale crystal growth experiments in which convection in the melt has been suppressed.

The purpose of this paper is to present theoretical results from computer-aided analysis of the interactions of natural convection and melt/solid interface shape in setting dopant distributions in crystals grown in a vertical Bridgman system. The prototype growth system considered here is shown in Figure 1 and consists of crystal and melt contained in a cylindrical ampoule of radius R and length L pulled slowly through a vertically aligned furnace with hot and cold isothermal zones. The isothermal zones are separated by an adiabatic region designed to promote steep axial temperature gradients and to maintain a flat solidification interface. Heat transfer in the Bridgman system without convection is well understood. A host of one- and two-dimensional heat transfer models [20-27] have been used to analyze the magnitudes of axial and radial temperature gradients in the gradient zone and the shape of the melt/solid interface. No previous studies have considered the effect of convection on melt/solid interface shape.

Convection in the Bridgman system is driven by buoyancy differences induced by radial and axial temperature gradients and may be either laminar, perfectly time-periodic or turbulent, depending on the magnitude of the temperature gradient, the size of the ampoule and its orientation with respect to the direction of gravity. When the melt is positioned below the crystal the axial temeperature gradient places the hottest (and less dense) melt on the bottom of the ampoule and is destabilizing. Kim et al. [5] used dopant striations in gallium-doped germanium crystals to identify melt lengths at which each of the three forms of convection were present. Others [8, 28] have oriented the melt above the crystal in order to produce a stably-stratified axial density gradient. Convection still exists in this configuration; radial temperature gradients introduced by changes in lateral heat transfer conditions cause lateral density variations that can drive laminar and even turbulent convection, as demonstrated in [29].

The adverse effects of large amplitude convection, especially time-dependent flows, on dopant segregation in the crystal are so severe that solidification experiments have been performed in outer space [30, 31] to test the feasibility of crystal growth in a reduced gravity environment. Even these experiments are not convectionless because time-averaged accelerations with magnitude as large as 10^{-4} the gravitational acceleration on earth still exist on board most spacecraft. As discussed below, the differences in space experiments may cause larger concentration variations than seen in crystals grown on earth.

The calculations described here are of the axisymmetric steady state velocity, temperature, and concentration fields and melt/solid interface shapes for the model of the vertical Bridgman system described in Section 2. The mathematical free-boundary problem that describes these variables is solved by a newly developed [31, 32] finite-element/Newton technique that computes simultaneously the shape of the solidification interface, the velocity and pressure fields in the melt and the temperature distribution in both melt and crystal. The increased efficiency of this algorithm over any other developed before [31] makes possible the wide range of calculations presented here. Also, as described in [32], the use of Newton's method for solution of the full set of nonlinear algebraic equations makes available powerful algorithms for detecting either the loss of solution or the existence of multiple solutions to the free-boundary problem represented by the finite-element equations.

Flow fields calculated with the finite-element/Newton algorithm are used in a separate calculation of the distribution of a dilute dopant within the melt and crystal. All the numerical methods are presented in detail elsewhere and so are only sketched in Section 3.

Flow fields and concentration distributions in the vertically stabilized (melt on top) configuration are presented in Section 4 along with sensitivity analysis for the length of the melt, the size of the gradient zone and the ratio of thermal conductivities between melt and solid. The usefulness of the concept of a diffusion-layer thickness for correlating the segregation results is addressed in Section 4.2. The flow patterns and segregation results predicted for this growth configuration are compared in Section 5 to results for the vertically destabilized (melt on bottom) arrangement. The bulk of the calculations reported here are for a melt and crystal with thermophysical properties similar to those of the gallium-doped germanium system used in several small-scale experiments [5, 8, 29]. The predictions of melt/solid interface shape, radial dopant profiles and effective axial segregation coefficients are used to establish the link between the calculations and experimentally observable quantities.

2. PROTOTYPE OF VERTICAL BRIDGMAN GROWTH SYSTEM

The finite length of a real ampoule in a Bridgman furnace causes the heat and mass transfer inside the sample to be time dependent for any nonzero translation rate. These transients are caused by the steady decrease in the ratio of melt to crystal in the ampoule and are slow for the growth rates typical for semiconductor materials. We replace the true unsteady problem with a prototype steady state process viewed from a stationary reference frame and described in the cylindrical polar coordinate system shown in Figure 1. The translation of the ampoule is accounted for by supplying melt into the ampoule at $z = 0$ with velocity $\tilde{v}_z = V_\ell$ and removing crystal at the other end of the ampoule at the rate $V_s \equiv (\rho_s/\rho_\ell)V_\ell = \sigma V_\ell$.

For long ampoules and melts with low Prandtl numbers, the transient effects on heat transfer are small [26] and the changes in the fluid mechanics are accurately accounted for by the steady state model with calculations for a succession of ampoule positions inside the furnace, each of which corresponds to a different time in the actual growth experiment. Changes in the length of the melt caused by translating the ampoule lead to transients in dopant transfer that force the average concentration of dopant over the cross section of the crystal to change with time. Our hypothetical steady state model for mass transfer ignores this effect. The prediction of effective segregation coefficients caused by convection from the results of the steady state model is addressed in Section 4.2.

The field equations governing heat transfer in both phases and fluid flow in the melt are put in dimensionless form by scaling lengths with the height of the ampoule L, velocity $\underset{\sim}{v}(r,z)$ with α_ℓ/L where α_ℓ is the thermal diffusivity in the liquid (see the list of thermophysical properties in Table I), pressure p(r,z) with $\rho_\ell\alpha_\ell^2/L^2$ and temperature $\theta(r,z) \equiv (\tilde{T}(r,z) - T_c)/(T_h - T_c)$. In this last definition $\tilde{T}(r,z)$ is the dimensional temperature field and T_c and T_h are the temperatures of the hot and cold regions of the furnace. In units of ampoule length, the dimensions of the ampoule and furnace are the aspect ratio of the ampoule $\Lambda \equiv R/L$, the length of the hot zone $L_h \equiv \tilde{L}_h/L$ and the length of the gradient region $L_g \equiv \tilde{L}_g/L$. These dimensionless scalings, especially the choice of L as the length scale, have been made for convenience and may not give dimensionless groups that are the most appropriate for the physics controlling the buoyancy-driven flow and associated dopant segregation. The formulation of more meaningful scaling is addressed in Section 4.5.

The location of the melt/solid interface is represented as $z = h(r)$, $0 \leq r \leq \Lambda$, and the unit vectors everywhere normal $\underset{\sim}{N}$ and tangent $\underset{\sim}{t}$ to the interface are

$$N \equiv \frac{\underset{\sim}{e}_z - h_r\underset{\sim}{e}_r}{(1 + h_r^2)^{1/2}} \quad , \qquad \underset{\sim}{t} = \frac{\underset{\sim}{e}_r + h_r\underset{\sim}{e}_z}{(1 + h_r^2)^{1/2}} \quad , \tag{1}$$

where $h_r \equiv dh/dr$ and the set $(\underset{\sim}{e}_r, \underset{\sim}{e}_\theta, \underset{\sim}{e}_z)$ are unit vectors for the cylindrical polar coordinate system.

Field variables in the melt $(0 \leq z \leq h(r), 0 \leq r \leq \Lambda)$ are governed by the axisymmetric and dimensionless form of the Boussinesq equations [32]:

$$\nabla \cdot \underset{\sim}{v} = 0 \tag{2}$$

$$\underset{\sim}{v} \cdot \nabla \underset{\sim}{v} = -\nabla p + Pr \nabla^2 \underset{\sim}{v} + RaPr\, \theta\, \underset{\sim}{e}_z \quad , \tag{3}$$

$$\underset{\sim}{v} \cdot \nabla \theta = \nabla^2 \theta \quad , \tag{4}$$

where $\nabla \equiv \underset{\sim}{e}_r \; \partial/\partial r + \underset{\sim}{e}_z \; \partial/\partial z$ is the gradient operator in cylindrical coordinates. The Prandtl Pr and Rayleigh numbers Ra appearing in eq. (3) are defined as $Pr \equiv \nu/\alpha_\ell$ and $Ra \equiv \beta g(T_h - T_c)L^3/\alpha_\ell \nu$ where the symbols are defined in Table II. The velocity field in the crystal is uniform at speed V_s and the temperature field in the crystal $(h(r) \leq z \leq 1,\ 0 \leq r \leq \Lambda)$ is governed by

$$Pe\, \underset{\sim}{e}_z \cdot \nabla \theta = \gamma \nabla^2 \theta \quad , \tag{5}$$

where $\gamma \equiv \alpha_s/\alpha_\ell$ is the ratio of thermal diffusivities in solid and melt and $Pe \equiv V_s L/\alpha_\ell$ is the Peclet number for convective heat transfer.

The shape of the melt/solid interface h(r) is set by the conditions for the equilibrium melting temperature $\tilde{T}_m$ and the balance of conductive heat fluxes across the interface with the latent heat released there. In dimensionless form, these interface conditions are

$$\theta(r,h(r)) \equiv (T_m - T_c)/(T_h - T_c) \quad , \tag{6}$$

$$(\underset{\sim}{N} \cdot \nabla \theta)_\ell - K\, (\underset{\sim}{N} \cdot \nabla \theta)_s = SPe\, (\underset{\sim}{N} \cdot \underset{\sim}{e}_z) \quad , \tag{7}$$

where $S \equiv \Delta H_f/\rho_\ell c_{p_\ell}(T_h - T_c)$ is the Stefan number and the subscripts in eq. (7) denote whether the interfacial flux is evaluated in the crystal (s) or the melt (ℓ).

Boundary conditions on velocity at the interface insure no slip tangential to the crystal and the solidification of melt at a rate proportional to the growth rate V_s and the difference between the densities $\sigma \equiv (\rho_s/\rho_\ell)$ of the two materials:

$$\underset{\sim}{v} \cdot \underset{\sim}{t} = Pe(\underset{\sim}{e}_z \cdot \underset{\sim}{t}) \quad , \quad \sigma(\underset{\sim}{v} \cdot \underset{\sim}{N}) = Pe(\underset{\sim}{e}_z \cdot \underset{\sim}{N}) \quad . \tag{8}$$

The top surface and sidewall of the ampoule are assumed to be no slip surfaces so that $v_r = 0$ and $v_z = \sigma Pe$ in the melt. The symmetry boundary conditions at the axis of the cylinder are

$$v_r = \partial v_z/\partial r = \partial \theta/\partial r = 0, \quad r = 0, \ 0 \leq z \leq 1 \quad . \tag{9}$$

The thermal boundary conditions along the ampoule are modelled after the idealized situation considered by Fu and Wilcox [2] in which the ampoule has negligible thermal mass, the adiabatic region is a perfect insulator and the heat transfer rates between the hot and cold regions of the furnace are so large that the ampoule has the temperature of the surrounding furnace. In addition, the ends of the ampoule are assumed to be perfectly insulated. None of these assumptions is totally realistic for small scale experimental systems. Actual ampoules provide resistance to radial heat transfer and conduct heat axially; this latter effect modifies axial temperature gradients [26] and causes radial temperature gradients near the melt/solid interface [27]. The mathematical forms of the thermal boundary conditions along the ampoule wall are stated in [32] and are not repeated here.

The differential mass balance equation appropriate for dilute dopants is

$$(Sc/Pr)\,\nabla\cdot(c\underset{\sim}{v}) = \nabla^2 c \quad , \tag{10}$$

where Sc ≡ $\nu/\mathcal{D}$ is the Schmidt number. The boundary conditions used for solving eq. (10) are

$$\underset{\sim}{N}\cdot\nabla c = (PeSc/Pr)(\underset{\sim}{e}_z\cdot\underset{\sim}{N})(1-k)c,\ 0 \leq r \leq \Lambda,\ z = h(r) \quad , \tag{11}$$

$$\partial c/\partial z = (PeSc/Pr)(c-1) \quad , \quad 0 \leq r \leq \Lambda \quad , \quad z = 0 \quad , \tag{12}$$

$$\partial c/\partial r = 0 \quad , \quad r = 0 = \Lambda \quad , \quad 0 \leq z \leq 1. \tag{13}$$

Equations (11) and (12) express conservation of mass at the melt/solid interface and the fictitious "inlet" at the melt end ($z=0$) of the ampoule, respectively. Equation (13) is the no flux condition valid at the centerline and sidewall of the ampoule. Once the velocity field in the melt and the shape of the melt/solid interface are determined from the two-phase natural convection problem described above, equations (10-13) reduce to a linear set to be solved for the concentration distribution throughout the melt.

3. FINITE ELEMENT ANALYSIS

The finite element/Newton technique developed in references [31-32] for solving steady solidification problems has been applied to the model of the vertical Bridgman system described by eqs. (1-9). First, finite element approximations to the velocities, pressure, temperature and melt/solid interface shape are combined with Galerkin's method to reduce the original partial differential equations and boundary conditions to a set of nonlinear algebraic equations. For an approximate location of the solidification isotherm h(r), melt and solid are divided into N_r radial and N_z axial elements; half of the axial elements are placed in each phase. A sample 4 x 16 ($N_r = 4$, $N_z = 16$) mesh is shown as Figure 2. The field variables are approximated by expansions of standard finite element basis functions and coefficients which are to be determined. We use mixed interpolation [33] for the Boussinesq equations with continuous bilinear polynomials for interpolating pressure and biquadratic ones for approximating temperature and velocities. The shape of the melt/solid interface h(r) is expanded in terms of Hermite cubic functions.

The field equations (2, 3, 5) are reduced by Galerkin's method to algebraic residual equations in terms of the unknown coefficients for each variable. The energy flux condition eq. (7) is incorporated into the residual equations for the energy equation (5) and the condition for the melting point isotherm eq. (6) along the solidification interface is distinguished as the equation for determining the interface location. A separate set of interface residual equations are formed from eq. (6) by applying Galerkin's method using the Hermite cubic polynomials as weighting functions; see [31]. The entire set of nonlinear algebraic equations for the field variables and interface shape are solved by Newton iteration as described in [30, 31]. Computer-aided methods for detecting and tracking multiple solutions to the algebraic equations are also described in [32].

The equations for mass conservation of a dopant (10-13) are also solved by the Galerkin finite element method with the concentration field $c(r,z)$ approximated by an expansion of unknown coefficients $\{c_i\}$ and biquadratic basis functions $\{\phi^i\}$

$$c(r,z) = \sum_{i=1}^{N_t} c_i \;\; \phi^i(r,t) \qquad , \tag{14}$$

where N_t is the total number of basis functions in the expansion. Linear algebraic equations result from applying Galerkin's method to eq. (10) and using the divergence theorem to incorporate the boundary conditions (11-13):

$$\sum_{i=1}^{N} A_{ij}\, c_j = b_i \qquad , \tag{15}$$

where

$$\begin{aligned} A_{ij} \equiv & \int_{V_\ell} [\phi^i \, \underline{v} \cdot \nabla\phi^j + \frac{Pr}{Sc} (\nabla\phi^i \cdot \nabla\phi^j)] \, dV \\ & + \int_{\mathcal{D}_I} Pe(1-k)(\underset{\sim}{e_z} \cdot \underset{\sim}{N})\phi^i\phi^j dA + \int_{\mathcal{D}_0} Pe\phi^i\phi^j dA \; , \end{aligned} \tag{16}$$

$$b_i \equiv \int_{\mathcal{D}_0} \phi^i \; Pe \; dA \qquad . \tag{17}$$

The nomenclature for the boundaries interface $\mathcal{D}_I$ and inlet $\mathcal{D}_0$ and the melt volume V_ℓ is shown on Figure 2. The equation set (15) is solved by Gaussian elimination and the resulting concentration fields are plotted as contours of c(r,z).

Although eqs. (10-13) yield a linear problem, the solution is by no means simple. The high velocities caused by natural convection and the low diffusivities of dopants in melts lead to convection dominated dopant transfer. This is clearly seen by computing a Peclet number for mass transfer in the melt as $Pe_m \equiv V^*L/\mathcal{D}$, where V* is the velocity scale for the convection. For natural convection driven by the vertical temperature gradient in the destabilized configuration, V* is $Ra^{1/2}\alpha_\ell/L$ and $Pe_m \equiv Ra^{1/2}Sc/Pr = 1 \times 10^5$ for a Rayleigh number of 1×10^4. Solution of the convection-diffusion problem (10-13) at this level of convection is one of the outstanding problems in numberical analysis [34, 35]. We have adopted two types of adaptive spacing of the finite element mesh to account for the steep concentration gradients that result from large Pe_m. First, each element of the finite element mesh for velocity and temperature is sub-divided into smaller sections for approximating c(r,z). Secondly, these small elements are not equally spaced but are graded to be smallest near the boundaries of the melt where the concentration varies most rapidly.

The stream function $\psi(r,z)$ for each velocity field is computed by solving the linear equation

$$\frac{1}{r}\frac{\partial^2\psi}{\partial r^2} - \frac{1}{r^2}\frac{\partial\psi}{\partial r} + \frac{1}{r}\frac{\partial^2\psi}{\partial z^2} = \frac{\partial v_r}{\partial z} - \frac{\partial v_z}{\partial r} \quad , \qquad (18)$$

by the Galerkin finite-element method with $\psi(r,z)$ represented in a biquadratic basis, just as for the concentration field eq. (14). We display flow fields in terms of streamlines plotted as contours of $\psi(r,z)$.

4. VERTICALLY STABILIZED CONFIGURATION

The large number of dimensionless thermophysical and geometrical parameters that must be set for any one simulation of the Bridgman system and the cost of each computation have forced us to concentrate on parameters similar to those for the gallium-doped germanium experiments underway in the Material Science Department at MIT [36]. The appropriate values of thermophysical parameters are listed in Table II and the corresponding dimensionless groups are given in Table I. The radius of the ampoule has been taken as 0.5 cm and the growth rate V_s has been set at 16 μm/sec. We first consider convection and segregation in the stabilized configuration (melt above crystal) with the ampoule four times longer than its radius, *i.e.*, $\Lambda = 0.25$.

This configuration and the values of the dimensionless groups listed in Table II are the basis of the calculations presented in Sections 4.1 - 4.3. The sensitivity of the results to the ratio of thermal conductivities and to the design of ampoule and furnace are considered in Sections 4.4 - 4.5.

4.1 Temperature and Velocity Fields

Calculations of large amplitude natural convection in melts with low Prandtl number are extremely difficult and the accuracy of the numerical approximations can only be systematically checked by refinement of the finite element mesh. We have used grids of 4 x 16, 6 x 24, and 8 x 32 elements to compute the flows in the base case described above for Rayleigh numbers ranging from 10 to 5×10^6. Streamlines and isotherms computed with the 8 x 32 mesh are shown on Figures 3 and 5 for the test case. With this mesh, 2398 nonlinear equations were solved by Newton's method; and each Newton iteration required 20 minutes of computer time in the Honeywell 6180 at MIT.

Three distinct types of flow patterns were observed. At low Rayleigh numbers ($Ra < 10^3$) the streamlines were rectilinear and only slightly distorted by buoyancy forces. For intermediate values of Ra ($10^3 \leq Ra \leq 10^6$) a cellular flow developed, which was driven by the radial temperature gradients established by the mismatch in thermal boundary conditions between the adiabatic and hot zones. The flow moved upward along the sidewall and downward at the centerlines of the ampoule. The center of the cell was located slightly above the gradient zone and migrated downward and toward the sidewall with increasing Ra. Increasing the Rayleigh number to 2.6×10^6 led to the development of a weak secondary cell adjacent to the melt/solid interface, as shown in Figures 3g and 3h; the onset of the multi-cellular flows marks the start of the third type of flow pattern. The motion in the secondary cell next to the interface is in the opposite direction to the main cell and leads to qualitatively different radial segregation than the flows with a single cell which exist for Ra less than 1×10^6. This point is discussed further below.

The three types of flows found with varying Rayleigh number are also distinguishable on the plot of the circular of the primary cell ψ_{max} shown as Figure 4. One interesting feature of this plot is that a part of the intermediate region can be identified where ψ_{max} is linear in Rayleigh number. This suggests that an exact linear analysis, such as performed for rotating flows by Harriott and Brown [12] and for buoyancy-driven flows in simpler geometries by Dressler [37], is applicable. Unfortunately, the temperature field in the melt, even in the absence of convection, is sufficiently complicated that closed-form calculations are impractical.

The temperature fields for several values of Rayleigh number are displayed in Figure 5 and show the effect of the low Prandtl number in the gallium-doped germanium system. For Rayleigh numbers between zero and 1×10^4, the thermal fields in both the melt and crystal are essentially the same as the field calculated without convection ($Ra = 0$) and are similar to results of Fu and Wilcox [21]. Increasing Ra above 1×10^4 caused the isotherms along the axis of the melt to compress toward the melt/solid interface by the downward fluid motion; by $Ra = 5 \times 10^6$ the shape of several isotherms farthest from the interface has inverted from convex to concave at the center of the melt. The isotherms in the crystal were unchanged by changing Ra. Also, the large portion of the crystal at the uniform temperature $\theta = 1$ pointed out that the length of ampoule in the cold portion of the furnace was sufficient to guarantee that the position of the end of the ampoule was unimportant.

The shape of the melt/solid interface is given by the isotherm $\theta = 0.5$ in Figure 5 and is plotted separately on Figure 6. As indicated by the temperature field the shape of the interface is unchanged by convection for Ra between 0 and 10^3. For higher Rayleigh numbers, the hot melt moving down the axis of the ampoule drove the melt/solid interface deeper into the adiabatic region. The changes in interface shape caused by convection are not large; even for $Ra = 5 \times 10^6$ the deflection of the interface is only six percent of its mean location.

The fine finite element mesh (8 x 32 elements) was necessary for quantitatively accurate calculations over the range $0 \leq Ra \leq 1 \times 10^6$ and for qualitatively accurate results above $Ra = 1 \times 10^6$. The accuracy of the calculations with the three different finite element grids was assessed by comparing results for ψ_{max} and by computing the degree of closure of the overall heat balance as a function of Rayleigh number. These results are tabulated in Table III. The heat balance was computed as

$$\Delta Q \equiv \int_{\mathcal{D}_M} (\underline{n} \cdot \nabla\theta) dA / Nu_I \quad , \tag{19}$$

where the integral was computed over all boundaries $\mathcal{D}_M$ surrounding the melt and Nu_I was the Nusselt number evaluted at the solidification interface $\mathcal{D}_I$:

$$Nu_I \equiv \int_{\mathcal{D}_I} (\underline{N} \cdot \nabla\theta) dA \quad . \tag{20}$$

Calculations with all three meshes gave heat balances that closed to within one percent of the interface flux and ψ_{max} values that were within one percent of the value for the 8 x 32 mesh when Ra was less than 1×10^4. The errors in ΔQ and ψ_{max} for the coarser meshes were larger at larger values of Ra.

A more serious problem with the coarse mesh occurred for Rayleigh numbers greater than 1×10^6. For both the 4 x 16 and 6 x 24 grids, sequences of calculations in increasing Ra failed to converge for values of Ra between 1×10^6 and 3×10^6. Techniques for detecting multiple steady solutions of algebraic equations described in another publication [32] were used to trace the families of steady solution through turns in Ra. The structure of these solutions is represented on Fig. 7 by plotting the Nusselt number Nu_I

as a function of Ra. For the 4 x 16 and 6 x 24 grids, three steady solutions to the algebraic solutions were found for several ranges of Rayleigh number.

These multiple solutions are bogus; refining the grid to 8 x 32 resulted in the single flow family described above and also represented on Fig. 7. The reason for the failure of the coarse mesh calculations is seen from the form of velocity field for Ra = 2.6×10^6. The small secondary cells that are created along the ampoule wall and at the melt/solid interface were not resolved by the 4 x 16 and 6 x 24 grids. Clearly, coarse calculations of large amplitude convection for low Prandtl number melts can give qualitatively wrong conclusions about the flow.

4.2 Dopant Segregation

Dopant fields were calculated for the velocity field and melt/solid interface shapes discussed above. The results reported here were calculated using a 18 x 34 mesh (2553 unknowns) embedded in the 8 x 16 grid used in the melt for computing the velocity field. The accuracy of the calculations of dopant concentration was assessed by computing the dopant mass balance for the entire melt; this balance closed to within five percent for Rayleigh numbers up to 1×10^4. The finite element grids used here were inadequate for dopant calculations at higher values of Ra.

Dopant fields computed for the segregation coefficient (k = 0.1) and Schmidt number (Sc = 10) similar to gallium in germanium are shown in Fig. 8. The almost parallel iso-concentration lines for Rayleigh numbers up to 10 correspond to the one-dimensional solidification model. The concentration field was deformed at higher values of Ra; flow downward along the axis swept dopant from the crystal and induced radial segregation across the surface of the crystal. The concentration field at Ra = 1×10^4 had the beginnings of the uniform core of melt and steep concentration gradients along each boundary which is consistent with the boundary-layer model for a well-mixed melt. A large amount of radial segregation was present even at this level of convection.

The radial variation of dopant composition at the interface is shown on Figure 9 for the concentration fields in Figure 7. The change in concentration across the interface evolved with increasing Ra from the approximately one percent segregation caused by interface curvature at Ra = 0 to almost seventy percent of the mean value 1/k for the worst case of Ra = 1×10^3. The radial variation in dopant decreased with the more intense flow motion that corresponded to Ra = 10^4. The maximum in radial segregation with increasing convection found here is consistent with calculations of Nikitan <u>et al.</u> [14] for the growth of gallium-doped germanium in a horizontal boat.

The percent radial segregation, defined as

$$\Delta c \equiv |c(0,h(0)) - c(\Lambda,h(\Lambda))| \times 100 \quad , \tag{21}$$

is plotted as a function of Ra on Figure 10 for segregation coefficients between 0.01 and 0.9. In all cases, Δc reached a maximum for the flow corresponding to nearly Ra = 10^3 and decreased for larger values of Rayleigh number. The value of the segregation coefficient set the mean concentration in the melt at the interface and affected the level of radial segregation in the crystal. The exponentially decreasing concentration profile present at low values of Ra extended further into the melt for smaller segregation coefficients and made the concentration field more sensitive to convection. Consequently the level of segregation Δc was higher for lower k.

Changing the diffusivity of solute also had a marked effect on the level of radial segregation, as is shown on Figure 11 by calculations of Δc for a range of Schmidt numbers and all other parameters the same as for the gallium-doped germanium system. Increasing Sc decreased the length of the concentration gradient at the interface and caused higher Peclet numbers ($Pe_M \equiv Ra^{1/2}Sc/Pr$) at lower values of Ra. The concentration fields for sample combinations of Sc and Ra are shown in Figure 12. At high Schmidt numbers and Rayleigh numbers of 1×10^3 and above, the isoconcentration curves develop fingers oriented parallel to the melt/solid interface that correspond to extremely rapid variation in composition within a distance of the same order of magnitude at the thickness of the diffusion-layer for ($Ra = 0$). This variation lead to large (over 100%) radial segregation.

4.3 Calculation of Effective Segregation Coefficients

The complicated segregation patterns discussed in the previous section create doubts as to the applicability of the simple "diffusion-layer" or "boundary-layer" model for correlating axial segregation behavior. Our detailed results for the velocity and dopant profiles put us in the rare situation of being able to check this correlation. To do this, radially averaged concentration profiles, defined as

$$\bar{c}(z) \equiv \int_0^{\Lambda} c(r,z)\, r dr \quad , \tag{22}$$

were calculated and plotted for each set of Ra, k, and Sc; sample profiles are shown in Figures 13 and 14 for Sc = 10 and Sc = 50, respectively. For low Rayleigh numbers ($0 \leq R \leq 1 \times 10^2$), these radially averaged profiles are essentially the same as the concentration profiles predicted by one-dimensional models which account only for the convection caused by crystal growth. A region of nearly uniform average concentration $\bar{c}(z) \doteq c_b$ developed with increasing Ra, as shown on Figure 13; here, the profile for Ra = 1×10^4 can be divided into a region of steep dopant gradient adjacent to the crystal, a zone of uniform concentration and a gradient zone caused by the fictitious inlet condition at $z - h(0) = 0$.

The effective segregation coefficient appropriate for a true unsteady Bridgman system with $\Lambda = 0.25$ was approximated as

$$k_{eff} = c_s/c_b \equiv 1/c_b \quad , \tag{23}$$

where c_s is the dimensionless average concentration across the crystal. Values of c_b and k_{eff} computed from the finite element results presented in the last section are summarized in Table IV.

If a diffusion-layer of thickness $\delta \equiv \tilde{\delta}/L$ exists that separates the crystal surface from bulk melt at concentration c_b, the effective segregation coefficient k_{eff} can be derived following Flemings [38] as

$$k_{eff} \equiv \frac{c_s}{c_b} \equiv \frac{k}{k + (1-k)\exp(-V_{\ell}\tilde{\delta}/\mathcal{D})} \quad , \tag{24}$$

or in the dimensionless form used here as

$$k_{eff} = \frac{k}{k + (1-k)exp(-\sigma\delta\ Pe\ Sc/Pr)} \quad . \qquad (25)$$

Rearranging eq. (25) yields an explicit relation for the diffusion-layer thickness δ:

$$\delta = -\frac{Pr}{PeSc\sigma} \ \ln \left\{ \frac{k}{k_{eff}} \cdot \frac{(1 - k_{eff})}{(1-k)} \right\} . \qquad (26)$$

Values of δ computed from eq. (25) with k_{eff} calculated from the finite element results are compared in Table IV to values δ_f measured from the profiles of $\overline{c}(z)$. In each case δ and δ_f are of the same order of magnitude but may differ by as much as a factor of two. This result is not surprising; within the distance δ_f from the crystal in the finite element calculations, the velocity field is a combination of the growth velocity and a contribution from natural convection. These two components are of the same order of magnitude and it is the latter component which causes the discrepancy between δ and δ_f and which leads to radial segregation.

4.4 Variation of Thermal Conductivities: $K \equiv k_s/k_\ell$

The ratio of thermal conductivities $K \equiv k_s/k_\ell$ is seldom unity for real materials, as has been assumed in the calculations presented above. Metallic semiconductors usually have higher conductivities in the melt ($K < 1$), while oxide systems usually have greater conductivities in the solid phase ($K > 1$). We have examined the effect of varying the conductivity ratio by changing K to 0.5 and 2.0. Temperature fields are shown in Figure 15 for these two cases at Ra = 1×10^4 and are essentially the same as for lower values of Rayleigh number. Changing K from unity destroyed the axial symmetry in the temperature field and displaced the interface from the center of the adiabatic zone. For $K = 0.5$, the melt penetrated deeper into the ampoule and the interface was convex toward the crystal. The interface was concave for $K = 2.0$ and located above the center of the adiabatic zone. In each case, the deflections of the interface were nearly ten percent of the mean location compared to the four percent deflections calculated when the conductivity ratio was unity.

Flow fields are displayed in Figure 16 for $K = 0.5$ and 2.0 and Rayleigh numbers between zero and 1×10^4. The changes in conductivities have little effect on the flow pattern besides the small deflection in the flow near the solidification interface needed because of the higher curvature of the crystal surface. The concentration fields shown on Figure 17 are much more distorted by the interface curvature; at low convection levels ($0 \leq Ra \leq 1 \times 10^2$) significant radial segregation occurred, as marked by the intersection of iso-concentration curves with the interface. The higher interfacial dopant concentrations appeared where the interface had its largest positive curvature as measured from the melt; this point shifted from the centerline for $K = 0.5$ to the wall of the ampoule for $K = 2.0$. The amount of radial segregation Δc caused solely by interface curvature was 23% for $K = 0.5$ and 18% for $K = 2.0$.

Fluid motion caused by natural convection swept dopant from the center of the interface towards the ampoule wall. For $K = 0.5$, weak convection decreased the radial segregation by stripping away the dopant peak caused by interfacial curvature. Cellular convection in the melt increased the radial segregation for the case with $K = 2.0$ by adding to the layer of dopant already at the edge of the crystal. These results are summarized on Figure 18 as a plot of Δc as a function of Ra.

4.5 Variation of Melt and Adiabatic Zone Lengths

The radial temperature gradients that drive natural convection in the vertically stabilized Bridgman configuration are not physically modelled by the Rayleigh number $Ra \equiv \beta g L^3 (T_h - T_c)/\alpha_\ell \nu$ scaled with the length of the ampoule. In fact, the structure of the flow should be independent of ampoule length as long as the flow cell does not interact with the top ($z = 0$) of the ampoule. The size of the radial temperature gradients will be proportional to that of the axial gradient in the gradient zone $(T_h - T_c)/\tilde{L}_g$ and so a more physically correct measure of the buoyancy driving force is

$$Ra_r \equiv \frac{\beta g[(T_h - T_c)/\tilde{L}_g]R^4}{\alpha_\ell \nu} = Ra\left(\frac{R}{L}\right)^3\left(\frac{L}{\tilde{L}_g}\right) = \frac{Ra\Lambda^3}{L_g} \quad . \tag{27}$$

Calculations were performed for melt lengths of 2R, 3R and 4R, with the crystal length and all other dimensionless groups held at the values of the base case studied above; the overall ampoule lengths L were 4R, 5R and 6R, respectively. The intensity of the convection as measured by Ra_r was held constant for each aspect ratio of the melt. Temperature, velocity and dopant fields are shown in Figure 19 for $Ra_r = 1.5625$, which corresponds to $Ra = 1 \times 10^3$ for the base case $\Lambda = 0.25$. It is clearly seen that these three fields are essentially identical for all three aspect ratios. The aspect ratio $\Lambda = 0.25$ is adequate for modelling much longer ampoules.

The calculations presented in Sections 4.1 - 4.3 show that radial segregation results from the interaction of the cellular flow driven by the radial temperature gradients at the edge of the adiabatic zone with the concentration gradient adjacent to the melt/solid solid interface. Hence, the length $L_g \equiv \tilde{L}_g/L$ of the adiabatic zone should be an important variable in determining the extent of this segregation. Calculations were performed for an ampoule with aspect ratio $\Lambda = 1/8$ and adiabatic zones with dimensions L_g of 1/8 (same as in Sections 4.1 - 4.3), 1/4, 3/8, and 1/2.

Samples isotherms, streamlines and concentration fields are shown in Figure 20 for $Ra = 8.0 \times 10^3$ and the thermophysical properties corresponding to the gallium-doped germanium system listed in Table II. As the length of the gradient region was increased the center of the cellular flow moved with the edge of the adiabatic region and was located farther from the melt/solid interface. For the longest gradient zone $L_g = 1/2$ (see Fig. 20d) the bulk of the convection occurred beyond the concentration gradient emanating from the melt/solid interface and the concentration field there was only slightly disturbed by the flow. Very little radial segregation is expected for these conditions. The percent radial segregation Δc is plotted on Fig. 20 as a function of Rayleigh number for the four values of L_g listed above.

Fixing Ra and increasing L_g corresponds experimentally to holding constant the overall temperature difference $(T_h - T_c)$ and changing only the length of the adiabatic zone. This procedure <u>decreases</u> the temperature gradient in the melt and weakens the flows, as shown on Fig. 20 by the increased spacing of the isotherms and by the decrease of the circulation ψ_{max} with increasing L_g. Calculations with constant intensity of the convection requira fixing the radially-scaled Rayleigh number Ra_r (see eq. 27). Curves of constant Ra_r are shown on Fig. 21 and demonstrate the decrease in radial segregation with increasing L_g. At moderate convection levels the adiabatic zone can be made long enough that the cellular flow does not interact with the dopant diffusion-layer adjacent to the crystal. The minimum length for this coupling will be strongly dependent on the value of the diffusivity (Schmidt number), which sets the length of the concentration gradient; see Fig. 10.

5. VERTICALLY DESTABILIZED CONFIGURATION

When the melt is positioned below the crystal the vertical temperature gradient leads to unstable density stratification which enhances convection. Calculations were performed for the destabilized geometry over a range of Rayleigh number Ra with the thermophysical properties listed in Table II. The size of the ampoule was taken to be the same as the base case for the stabilized system, i.e. $L_g = 1.0$ and $\Lambda = 1/4$. For Rayleigh numbers up to $Ra = 1 \times 10^5$, the temperature fields for the destabilized configuration were indistinguishable from the one for pure conduction ($Ra = 0$; see Fig. 3a) and so are not shown here. Streamlines computed for four representative values of Ra are displayed as Fig. 22.

The direction of the flow in the destabilized system was opposite that for the stabilized configuration and had qualitatively different effects on melt/solid interface shape and solute segregation. Melt moved upward along the sidewall of the ampoule, turned inward at the melt/solid interface, and fell along the centerline of the melt. As in the stabilized geometry, three regimes of the flow were located with changing Ra. Cellular fluid motion developed near the centerline for low values of Rayleigh number and spread toward the ampoule wall with increasing Ra. The center of the cell was positioned near the edge of the adiabatic zone, indicating that the radial temperature gradients at this edge were influencing the flow. At $Ra = 1 \times 10^5$ (see Fig. 22d) the destabilizing axial temperature gradient was controlling the flow and the cell had migrated downward in the ampoule. Calculations in a similar flow geometry and low Prandtl number [31] have indicated that the destabilized flow will separate from the sidewall at higher Rayleigh numbers.

Melt/solid interface shapes are shown in Fig. 23 for the flow fields given in Figure 22. Again, conduction dominated the heat flux in the melt near the surface of the crystal and the shape of the solidification isotherm was only slightly altered by convection. The shape shown for Ra between 0 and 1×10^3 was the same as shown for the stabilized configuration and low Rayleigh numbers in Fig. 6. The hot melt rising along the ampoule wall pushed the interface higher into the adiabatic zone at Ra = 1×10^3 and above and resulted in interfaces with convection being "flatter" than the shape corresonding to Ra = 0. The maximum height of the interface for Ra = 1×10^5 occurred off the centerline of the ampoule.

More dramatic differences are found by comparing radial dopant profiles for the two geometries. Dopant fields and interface distributions are shown in Figs. 24 and 25 for the parameters listed in Table II. The flow upward to the interface swept dopant from the outer edges of the crystal to the center of the ampoule. This led to interfacial concentrations that were highest at the center of the crystal, see Fig. 24. The amount of radial segregation across the crystal decreased for Ra = 1×10^4, just as in the case of the stabilized configuration. The percent radial segregation expected in the stabilized and destabilized geometries are compared directly on Fig. 26. The maximum in radial segregation is twenty percent less for the destabilizing configuration than for the stabilized system.

6. DISCUSSION

The coupled analysis of natural convection, melt/solid interface shape and dopant segregation in small-scale crystal growth systems is complicated, but is no longer impossible, because of the advent of new finite-element methods. The detailed pictures of the field variables and solidification front for the vertical Bridgman system studied here give new insights into the role of convection in setting the effective segregation between the bulk melt and crystal and the radial segregation in the crystal.

For moderate levels of convection, the stagnant-film or diffusion-layer model is a gross over-simplification of these interactions. Diffusion-layer thicknesses δ determined from eq. (26) and experimental data are, at best, an empirical fit to the effective segregation coefficient for the crystal/melt system. The comparison in Section 4.3 demonstrates that, although the radially averaged diffusion-layer thickness determined from the finite element simulations and eq. (26) are of the same order-of-magnitude, the actual concentration gradient adjacent to the crystal is far from radially uniform. As much as sixty percent radial segregation can exist. Only detailed calculations of the exact interaction of fluid flow and the dopant profile adjacent to the interface can be used to estimate the level of radial segregation in the crystal.

Our study of a prototype Bridgman system gives qualitative understanding of fluid flow and dopant segregation in actual growth systems and will serve as the starting point for more refined calculations aimed directly at comparison with experiments in a well-characterized small-scale system [36]. In these calculations, the ratio of thermal conductivities K between melt and crystal and the length of the gradient zone $\tilde{L}_g$ have emerged as important design parameters for determining interface shape and radial segregation. The value of K sets the shape of the interface and determines the qualitative behavior of the radial segregation with increased convection. The length $\tilde{L}_g$ sets the degree of interaction between the cellular flow and the concentration gradient adjacent to the interface. For long enough gradient zones and moderate convection levels, the flow causes little radial segregation; see Fig. 21.

Accurate comparisons with experimentally determined interface shapes and radial and axial dopant profiles will require the inclusion of the temperature variations of key thermophysical properties, such as the melt and solid conductivities and the density of the melt. Most of these variations are unknown. The thermal interactions between the ampoule and the surroundings, e.g. heat capacity and conductivity of the ampoule, will also have to be more accurately accounted for to correctly model radial temperature gradients in the system.

The slow translation of the ampoule has little effect on the temperature and velocity fields, when the ampoule is sufficiently long; however, the average concentration of dopant in the melt will increase slowly with time. For convection levels intense enough that a plateau in $\bar{c}(z)$ forms in the melt (see Fig. 13), this transient can be studied by an unsteady dopant calculation with fixed melt length and steady fluid flow, but with a time varying inlet concentration determined by an overall mass balance. For very low convection levels and high diffusivities (low Sc) where the concentration gradient extends to the end of the ampoule, fully transient calculations taking into account the length of the melt will be necessary. Efficient numerical methods presently exist only for one-dimensional solidification problems [39] and are being extended to two-dimensional simulations.

The most critical issue not addressed in this paper is the transition from the steady-state flow patterns predicted here to time-periodic flows observed in some experiments [5, 29]. Mathematically, these transitions occur as Hopf bifurcations from the steady flows and have been predicted theoretically by computer-aided bifurcation analysis combined with finite-element calculations [40] for low Prandtl number melts in the horizontal boat geometry studied experimentally by Hurle et al. [41]. Simulation of crystal growth in the time-periodic regime requires time-dependent solution of the Bousinesq equations as performed by some researchers [14, 42] without the interaction with the melt/solid interface. Fully transient calculations are no panacea. Besides being extremely expensive, their accuracy is difficult to assess. The loss-of-existence of steady solutions shown in Section 4.1 for crude finite element approximations would be manifested as time-fluctuating flows in transient calculations. As is the case here, refined transient calculations may lead to steady velocity and temperature fields.

ACKNOWLEDGEMENTS

This research was supported by the Materials Processing Program of the U.S. National Aeronautics and Space Administration and by the Information Processing Services at Massachusetts Institute of Technology.

REFERENCES

[1] J.A. Burton, R.C. Prim, and W.P. Slichter, J. Chem. Phys. 21 (1953) 1987.

[2] L.O. Wilson, J. Crystal Growth 44 (1978) 371.

[3] L.O. Wilson, J. Crystal Growth 44 (1978) 247.

[4] C. Wagner, J. Metals 6 (1954) 154.

[5] K.M. Kim, A.F. Witt, M. Lichtensteiger, and H.C. Gatos, J. Electrochem. Soc. 125 (1978) 475.

[6] J.J. Favier, Acta Metallurgica 29 (1981) 197.

[7] J.J. Favier, Acta Metallurgica 29 (1981) 205.

[8] D.E. Holmes and H.C. Gatos, J. Electrochem. Soc. 128 (1981) 429.

[9] P.A. Clark and W.R. Wilcox, J. Crystal Growth 50 (1980) 461.

[10] N. Kobayashi and W.R. Wilcox, J. Crystal Growth 59 (1982) 616.

[11] W.R. Wilcox, unpublished manuscript, 1982.

[12] G.M. Harriott and R.A. Brown, J. Fluid Mech. 126 (1983) 269.

[13] G.M. Harriott and R.A. Brown, J. Crystal Growth, to be submitted.

[14] S.A. Nikitan, V.I. Polezhayev and A.I. Fedyushkin, J. Crystal Growth 52 (1981) 471.

[15] S.R. Coriell and R.F. Sekerka, J. Crystal Growth 46 (1979) 479.

[16] S.R. Coriell, R.F. Boisvert, R.G. Rehm and R.F. Sekerka, J. Crystal Growth 54 (1981) 167.

[17] H.M. Ettouney and R.A. Brown, J. Crystal Growth 58 (1982) 313.

[18] J.P. Kalejs, L.-Y. Chin, F.M. Carlson, J. Crystal Growth, in press (1983).

[19] H.M. Ettouney and R.A. Brown, J. Appl. Physics, submitted (1983).

[20] C.E. Chang and W.R. Wilcox, J. Crystal Growth 21 (1974) 135.

[21] T.-W. Fu and W.R. Wilcox, J. Crystal Growth 48 (1980) 416.

[22] T.W. Clyne, J. Crystal Growth 50 (1980) 684.

[23] T.W. Clyne, J. Crystal Growth 50 (1980) 691.

[24] P.C. Sukanek, J. Crystal Growth 58 (1982) 208.

[25] P.C. Sukanek, J. Crystal Growth 58 (1982) 219.

[26] T.J. Jasinski, W.M. Rohsenow, and A.F. Witt, J. Crystal Growth, in press (1983).

[27] T.J. Jasinski, Ph.D. Thesis, Massachusetts Institute of Technology, 1983.

[28] L. Morris and W. Winegard, J. Crystal Growth 5 (1969) 361.

[29] A.F. Witt, H.C. Gatos, M. Lichtensteiger, M.C. Lavine, and C.J. Herman, J. Electrochem. Soc. 122 (1975) 276.

[30] A.F. Witt, H.C. Gatos, M. Lichtensteiger, and C.J. Herman, J. Electrochem. Soc. 125 (1978) 1883.

[31] C.J. Chang and R.A. Brown, in: Proc. 2nd Natl. Symp. on Numerical Methods in Heat Transfer, Ed. T.-M. Shih (Hemisphere Press, New York, 1982).

[32] C.J. Chang and R.A. Brown, J. Computat. Physics, submitted (1982).

[33] P. Huyakorn, C. Taylor, R. Lee and P. Gresho, Computers and Fluids 6 (1978) 25.

[34] M.T. Van Genuchten and W.G. Gray, Intern. J. Numer. Meth. Eng. 12 (1978) 387.

[35] B.A. Finlayson, Nonlinear Analysis in Chemical Engineering, McGraw-Hill, New York, 1980.

[36] A.F. Witt, in Annual Report of the Materials Processing Center of MIT, 1981.

[37] R.F. Dressler, J. Crystal Growth 54 (1981) 523.

[38] M.C. Flemings, Solidification Processing, McGraw-Hill, 1974.

[39] J.J. Derby, E.B. Bourret, A.F. Witt and R.A. Brown, J. Crystal Growth, in preparation.

[40] C.J. Chang and R.A. Brown, Int. J. Num. Meths. Fluids, to be submitted (1983).

[41] D.T.J. Hurle, E. Jakeman and C.P. Johnson, J. Fluid. Mech. 64 (1974) 565.

[42] W.E. Langlois, Physicochemical Hydrodynamics 2 (1981) 245.

FIGURE CAPTIONS

Table I.	Dimensionless Parameters and Representative Values for the Gallium-Doped Germanium System.
Table II.	Material Properties Characteristic of Gallium-Doped Germanium.
Table III.	Accuracy of Finite Element Calculations of Flow and Temperature Fields.
Table IV.	Comparison of Effective Segregation Coefficients Predicted by Finite Element Analysis with Diffusion-Layer Model, Eq. (26).
Figure 1.	Geometry of prototype vertical Bridgman growth system.
Figure 2.	Sample finite element mesh for computing velocity and temperature fields and melt/solid interface shape.
Figure 3.	Sample flow fields for vertically stabilized Bridgman system with Rayleigh numbers between 0 and 2.5 x 10^6. Streamlines are spaced at equal intervals between the maximum (or minimum) value for the cell and zero.
Figure 4.	Maximum streamfunction ψ_{max} as a function of Ra for vertically stabilized Bridgman system.
Figure 5.	Sample temperature fields for the vertically stabilized Bridgman system with Rayleigh numbers between 0 and 2.5 x 10^6.
Figure 6.	Melt/solid interface shapes for the flow and temperature fields shown in Figs. 3 and 5.
Figure 7.	Change of structure with Rayleigh number of flow families for three finite element meshes, as represented by the Nusselt number Nu_ℓ.
Figure 8.	Dopant concentration fields for flow fields shown in Fig. 3; $k = 0.1$ and $Sc = 10$.
Figure 9.	Variation of interfacial dopant concentration with Rayleigh number, $k = 0.1$ and $Sc = 10$.
Figure 10.	Percent radial segregation as a function of Rayleigh number and segregation coefficient for the vertically stabilized Bridgman system; $Sc = 10$.

Figure 11.	Percent radial segregation as a function of Rayleigh number and Schmidt number for the vertically stabilized Bridgman system; $k = 0.1$.
Figure 12.	Dopant concentration fields for three Schmidt numbers as a function of Rayleigh number; $k = 0.1$.
Figure 13.	Profiles of radially averaged dopant concentration for three values of Ra; $k = 0.1$ and $Sc = 10$.
Figure 14.	Profiles of radially averaged dopant concentration for three values of Ra; $k = 0.1$ and $Sc = 50$.
Figure 15.	Sample temperature fields for vertically stabilized Bridgman systems with $Ra = 1 \times 10^4$ and thermal conductivity ratios of (a) $K = 2.0$ and (b) $K = 0.5$. All other parameters are the same as listed in Table I.
Figure 16.	Sample flow fields for vertically stabilized Bridgman systems with thermal conductivity ratios of (a-d) $K = 0.5$ and (e-f) $K = 2.0$.
Figure 17.	Dopant concentration fields for flow fields shown in Figure 16; $k = 0.1$ and $Sc = 10$.
Figure 18.	Percent radial segregation as a function of Rayleigh number and thermal conductivity ratio; $k = 0.1$ and $Sc = 10$.
Figure 19.	Effect of melt length on temperature, velocity and dopant fields for $Ra_r = 1.5625$, $k = 0.1$ and $Sc = 10$.
Figure 20.	Effect of the length of the gradient zone L_g on temperature, velocity and dopant fields for $Ra = 1 \times 10^3$, $k = 0.1$ and $Sc = 10$.
Figure 21.	Effect of the length of the gradient zone L_g on the percent radial segregation Δc; $k = 0.1$ and $Sc = 10$.
Figure 22.	Sample flow fields for vertically destabilized Bridgman system with the thermophysical properties given in Tables I and II.
Figure 23.	Melt/solid interface shapes for the flow fields shown in Fig. 22.
Figure 24.	Dopant concentration fields for flow fields shown in Fig. 22; $k = 0.1$ and $Sc = 10$.

Figure 25	Variation of interfacial dopant concentration with Rayleigh number; $k = 0.1$ and $Sc = 10$.
Figure 26	Comparison of percent radial segregation for stabilized and destabilized Bridgman systems; $k = 0.1$ and $Sc = 10$.

Table I. Dimensionless Parameters and Representative Values for Gallium-Doped Germanium System

GROUP	DEFINITION	VALUE
Rayleigh Number	$Ra \equiv \beta g(T_h - T_c)L^3/\alpha_\ell \nu$	$0 - 10^7$
Prandtl Number	$Pr \equiv \nu/\alpha_\ell$	0.01
Peclet Number	$Pe \equiv V_s L/\alpha_\ell$	0.01
Conductivity Ratio	$K \equiv k_s/k_\ell$	1.0
Stefan Number	$S \equiv \Delta H_f/\rho_\ell c_{p_\ell}(T_h - T_c)$	1.0
Schmidt Number	$Sc \equiv \nu/\mathcal{D}$	10
Thermal Diffusivity Ratio	$\gamma \equiv \alpha_s/\alpha_\ell$	1.0
Density Ratio	$\sigma \equiv \rho_s/\rho_\ell$	1.0

Table II. Material Properties Characteristic of Gallium-Doped Germanium

Property	Value
Thermal conductivity of melt (k_ℓ)	0.17 W/K cm
Thermal conductivity of solid (k_s)	0.17 W/K cm
Heat capacity of melt (c_{p_ℓ})	0.17 J/gm K
Heat capacity of solid (c_{p_s})	0.17 J/gm K
Density of melt (ρ_ℓ)	5.6 g/cm^3
Density of solid (ρ_s)	5.6 g/cm^3
Melting temperature (T_M)	958°C
Kinematic Viscosity of Melt (ν)	0.13 cm^2/sec
Heat of fusion (ΔH_s)	506 J/gm
Thermal Expansion Coefficient (β)	0.25×10^{-3} (K)$^{-1}$
Diffusivity of Ga in Ge ($\mathcal{D}$)	1.3×10^{-4} cm^2/sec
Segregation Coefficient of Ga in Ge (k)	0.1

Table III. Accuracy of Finite Element Calculation of Flow and Temperature Fields

RAYLEIGH NUMBER	MAXIMUM VALUE OF ψ ψ_{max}			ERROR IN HEAT BALANCE $\Delta Q \times 100\%$		
	4 x 16	6 x 24	8 x 32	4 x 16	6 x 24	8 x 32
0	—	—	—	1.01	0.86	0
1×10^1	—	—	—	1.00	0.86	0
1×10^2	—	—	—	1.00	0.86	0
1×10^3	7.83×10^{-4}	7.78×10^{-4}	7.78×10^{-4}	0.99	0.64	0.74
1×10^4	6.08×10^{-3}	6.02×10^{-3}	6.01×10^{-3}	0.62	0.59	0.54
1×10^5	3.18×10^{-2}	3.57×10^{-2}	3.59×10^{-2}	1.86	1.19	0.86
1×10^6	1.23×10^{-1}	1.19×10^{-1}	1.29×10^{-1}	7.59	5.64	4.55

Table IV. Comparison of Effective Segregation Coefficients Predicted by Finite Element Analysis with Diffusion-Layer Model.

k	Sc	c_b		$k_{eff} \equiv 1/c_b$		δ, eq. (26)		δ_f (FEM)	
		$Ra=10^3$	$Ra=10^4$	$Ra = 10^3$	$Ra = 10^4$	$Ra = 10^3$	$Ra = 10^4$	$Ra = 10^3$	$Ra = 10^4$
0.1	10	5.40	8.40	0.19	0.120	0.070	0.020	0.125	0.025
0.1	50	2.05	6.00	0.49	0.175	0.040	0.012	0.042	0.020
0.01	10	50.0	80.00	0.02	0.013	0.070	0.027	0.125	0.041
0.50	10	1.50	1.80	0.75	0.550	0.110	0.020	0.108	0.031

ORIGINAL PAGE IS
OF POOR QUALITY

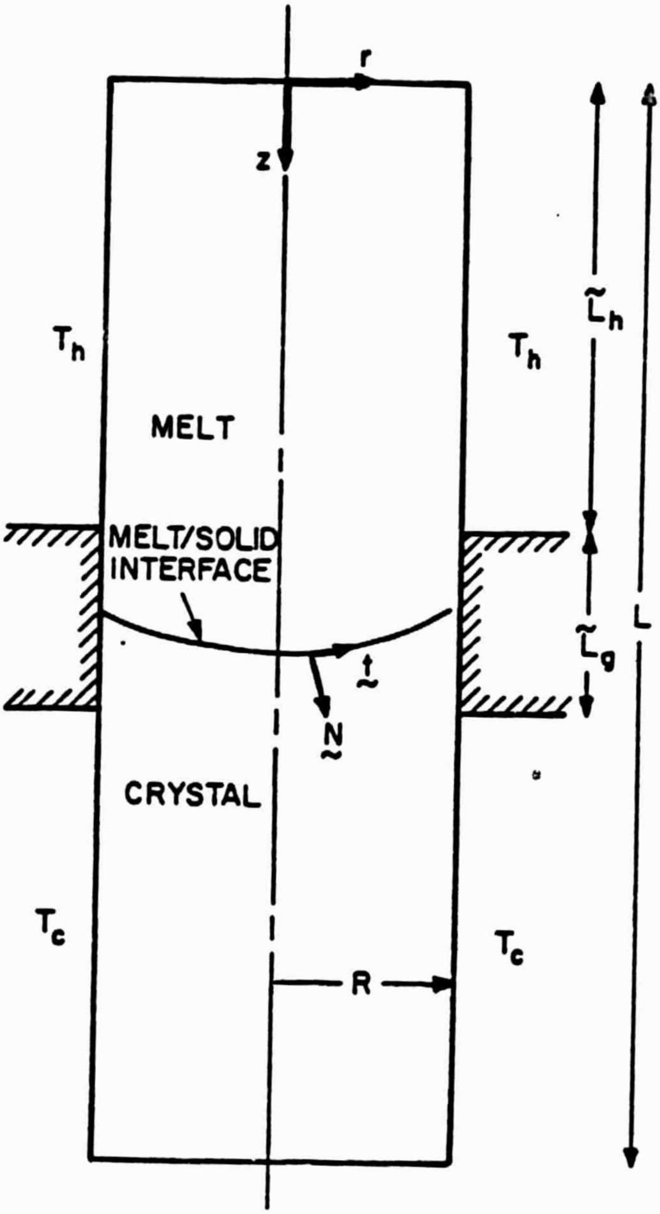

Figure 1

Chang and Brown

ORIGINAL PAGE IS
OF POOR QUALITY

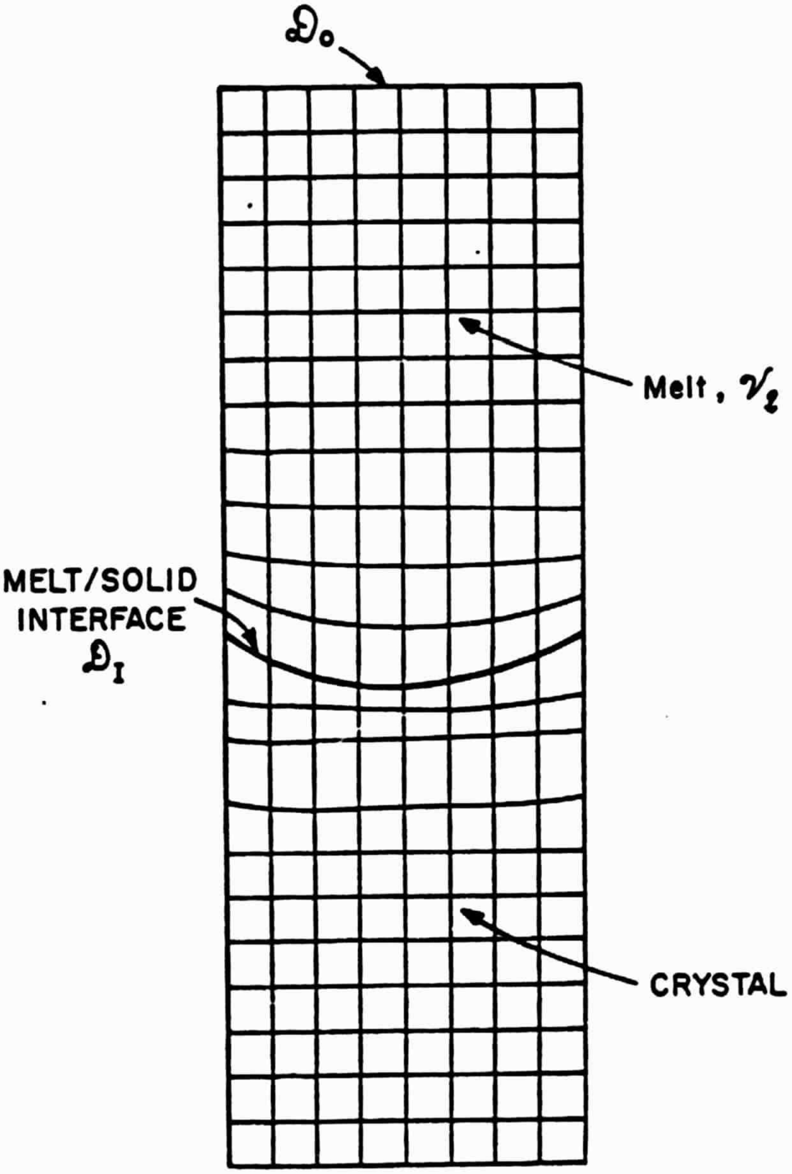

Figure 2

Chang and Brown

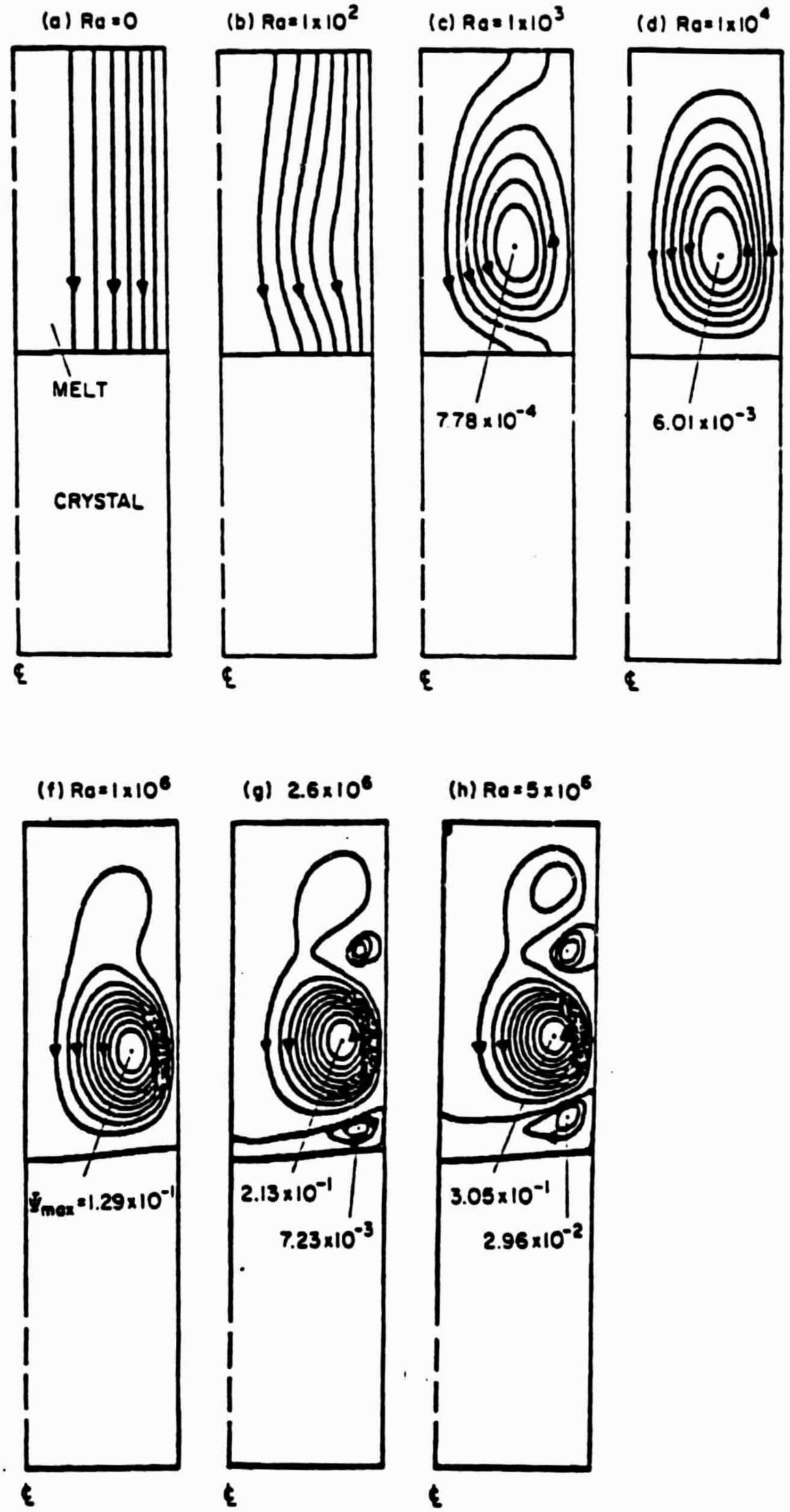

Figure 3

Chang and Brown

ORIGINAL PAGE IS
OF POOR QUALITY

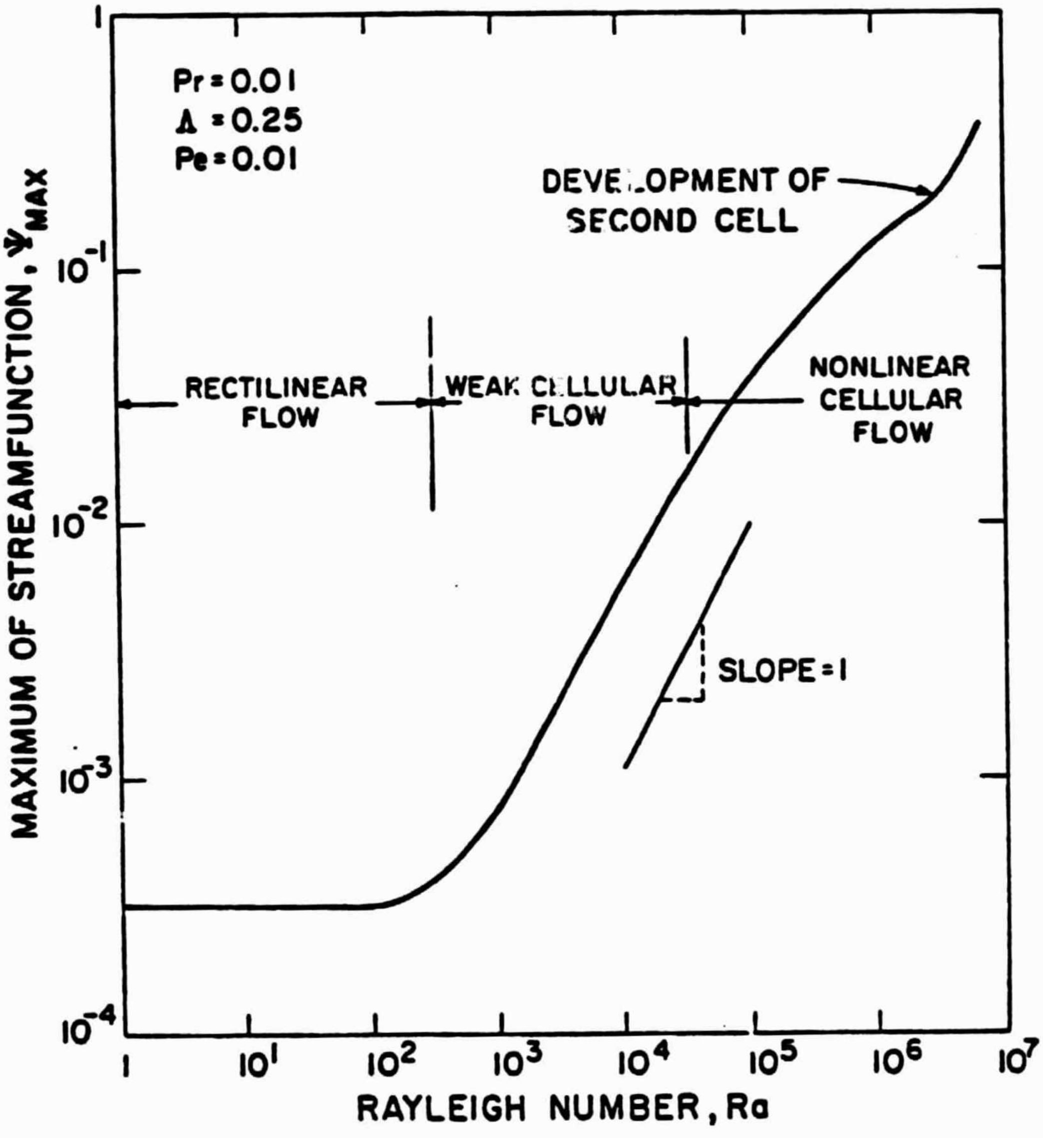

Figure 4

Chang and Brown

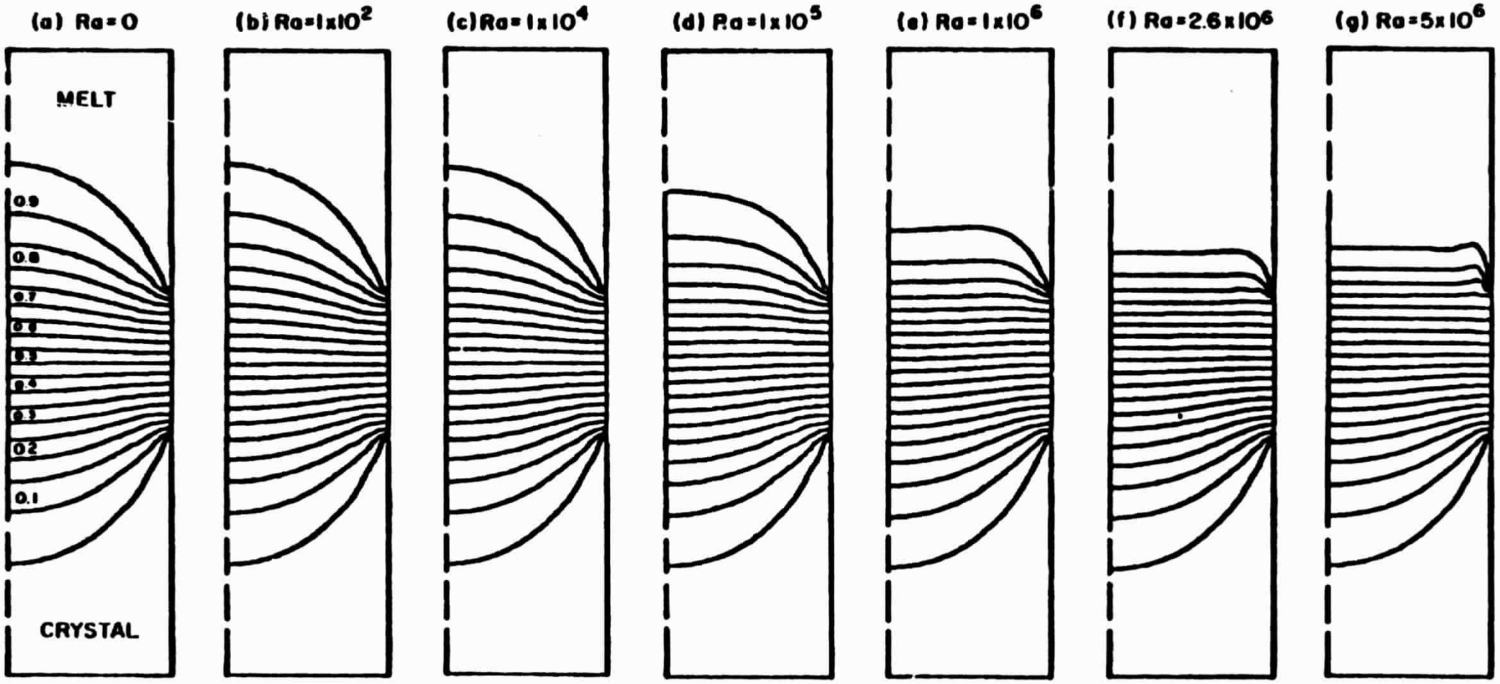

Figure 5

Chang and Brown

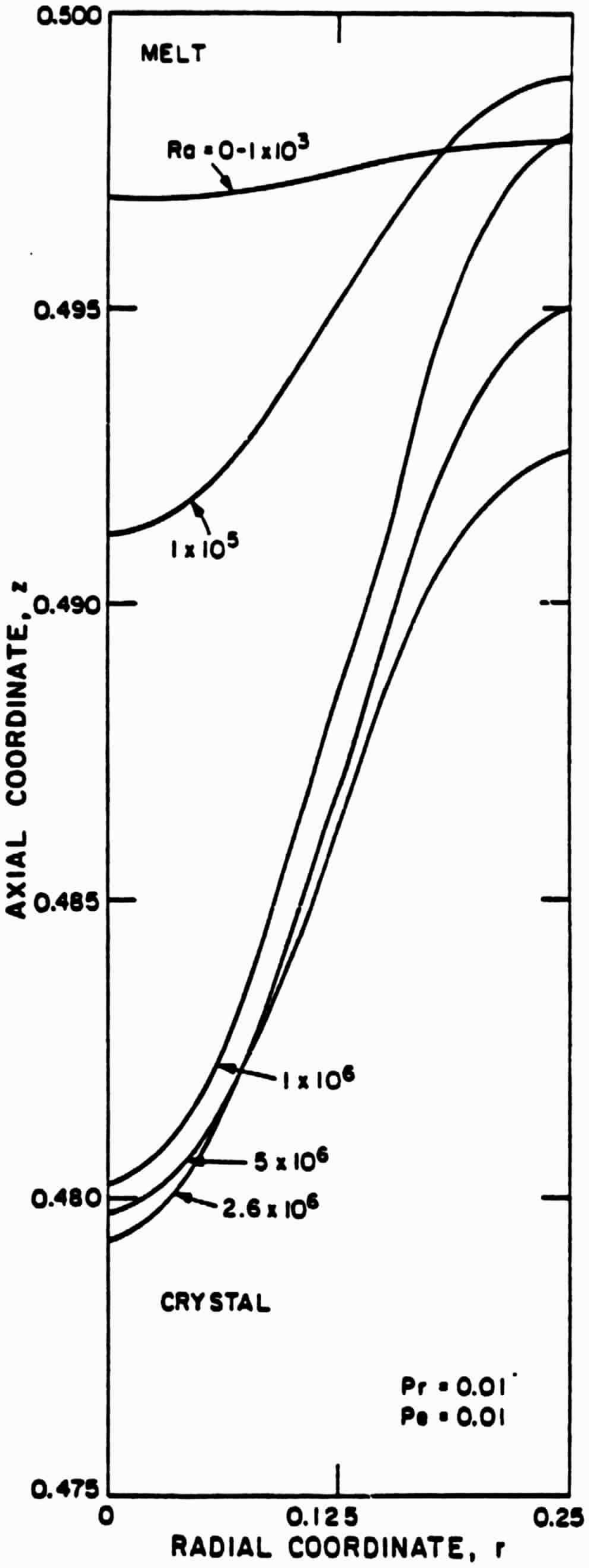

Figure 6

Chang and Brown

ORIGINAL PAGE IS
OF POOR QUALITY

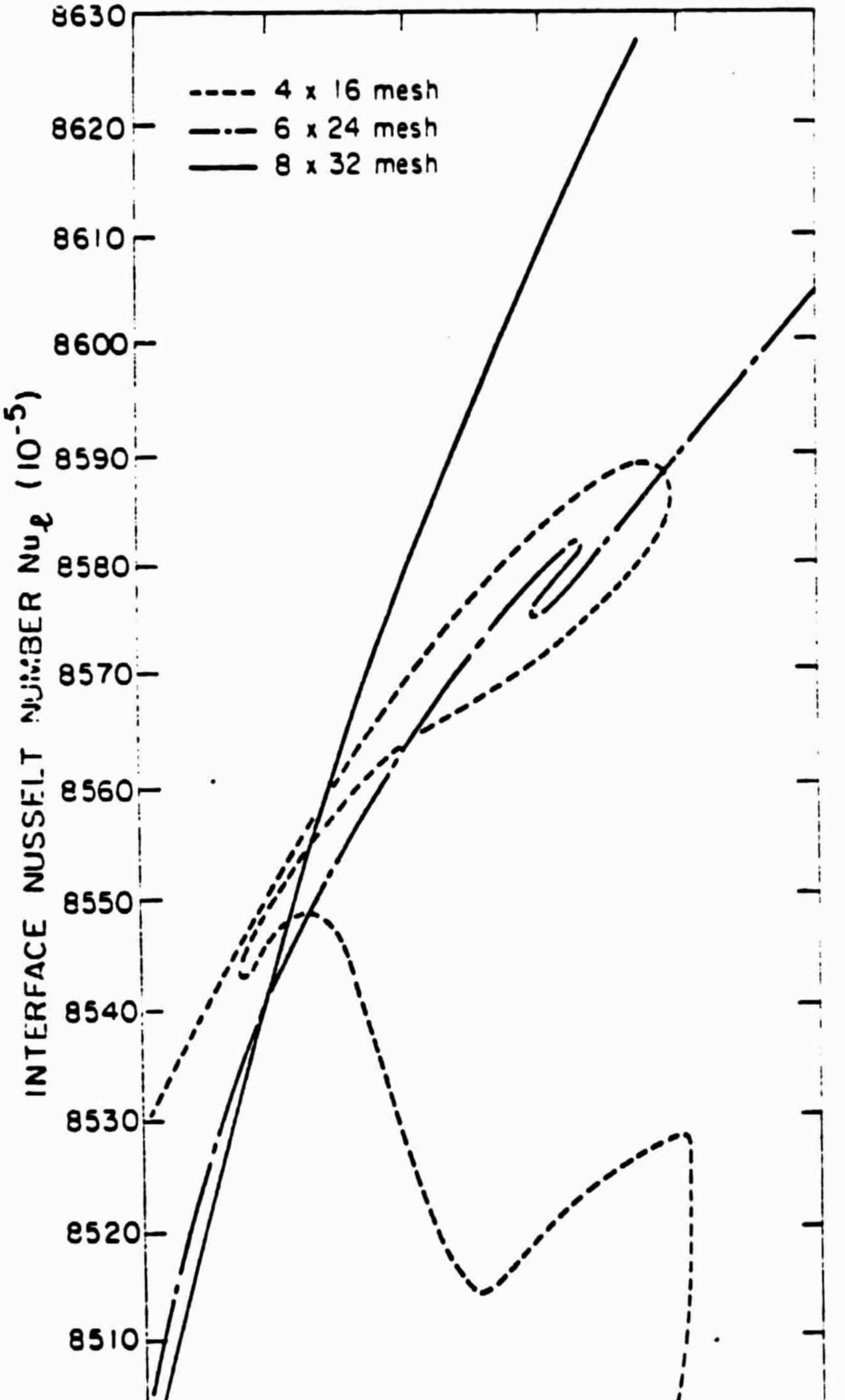

Figure 7
Chang and Brown

ORIGINAL PAGE IS
OF POOR QUALITY

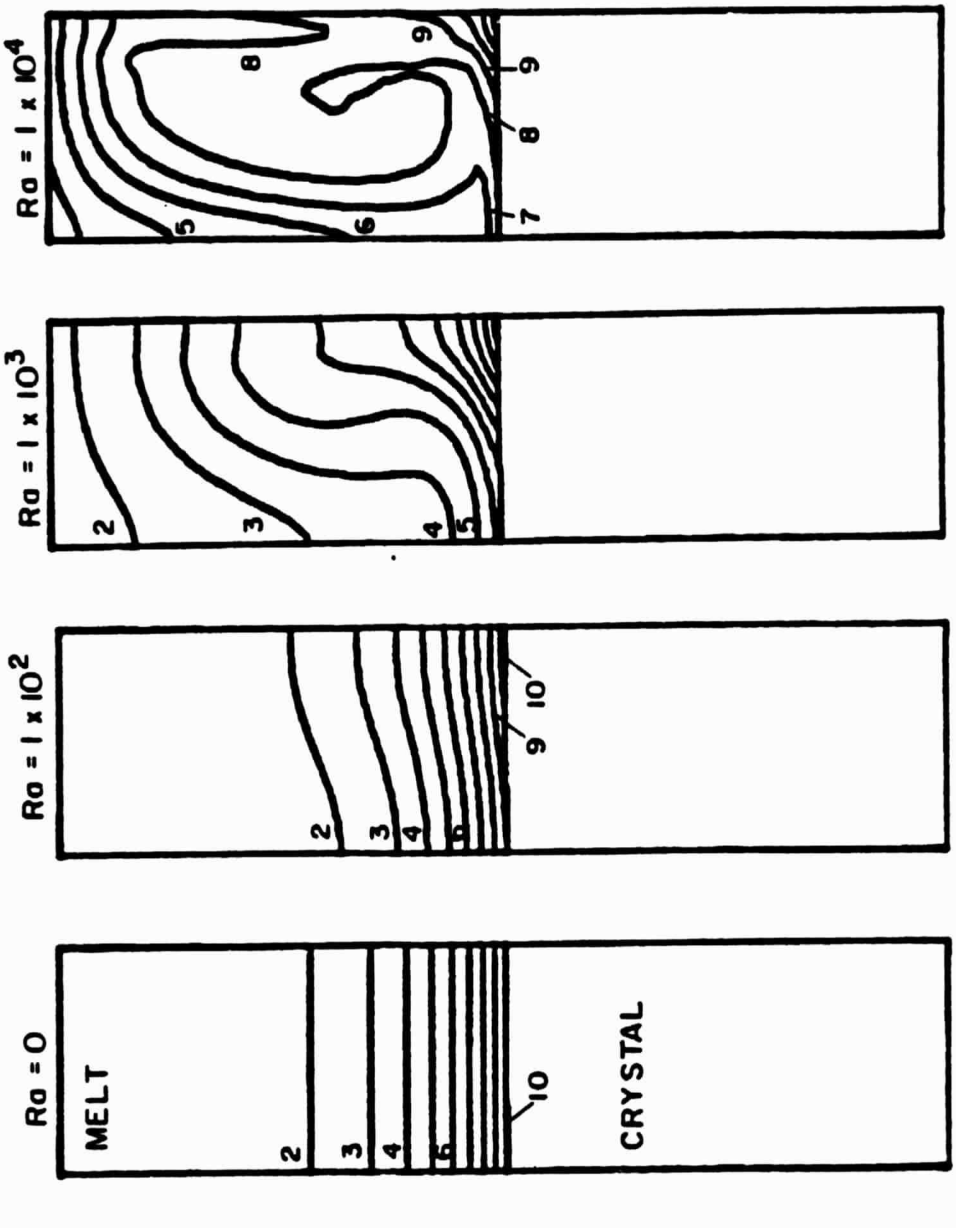

Chang and Brown

Figure 8

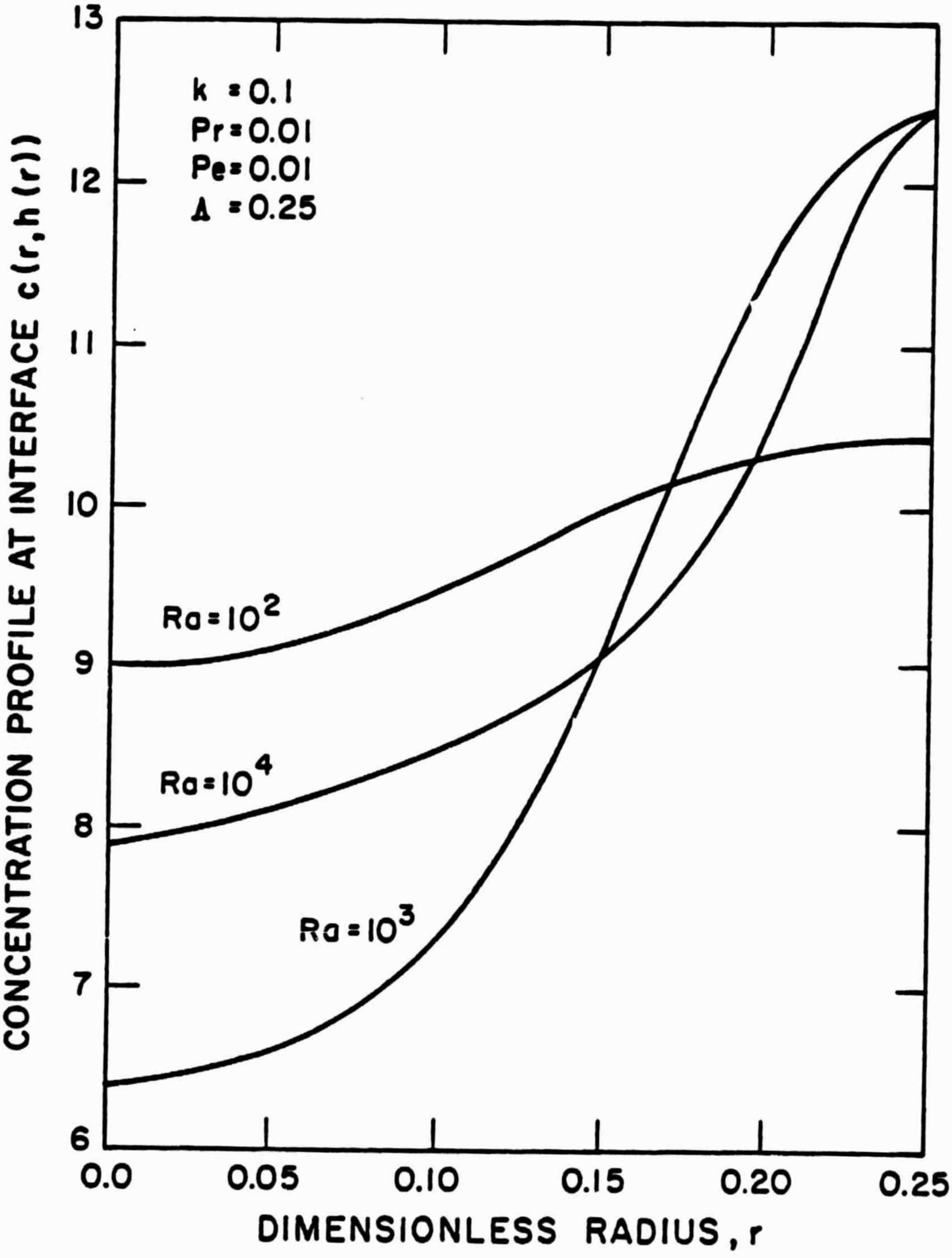

Figure 9
Chong and Brc

ORIGINAL PAGE IS
OF POOR QUALITY

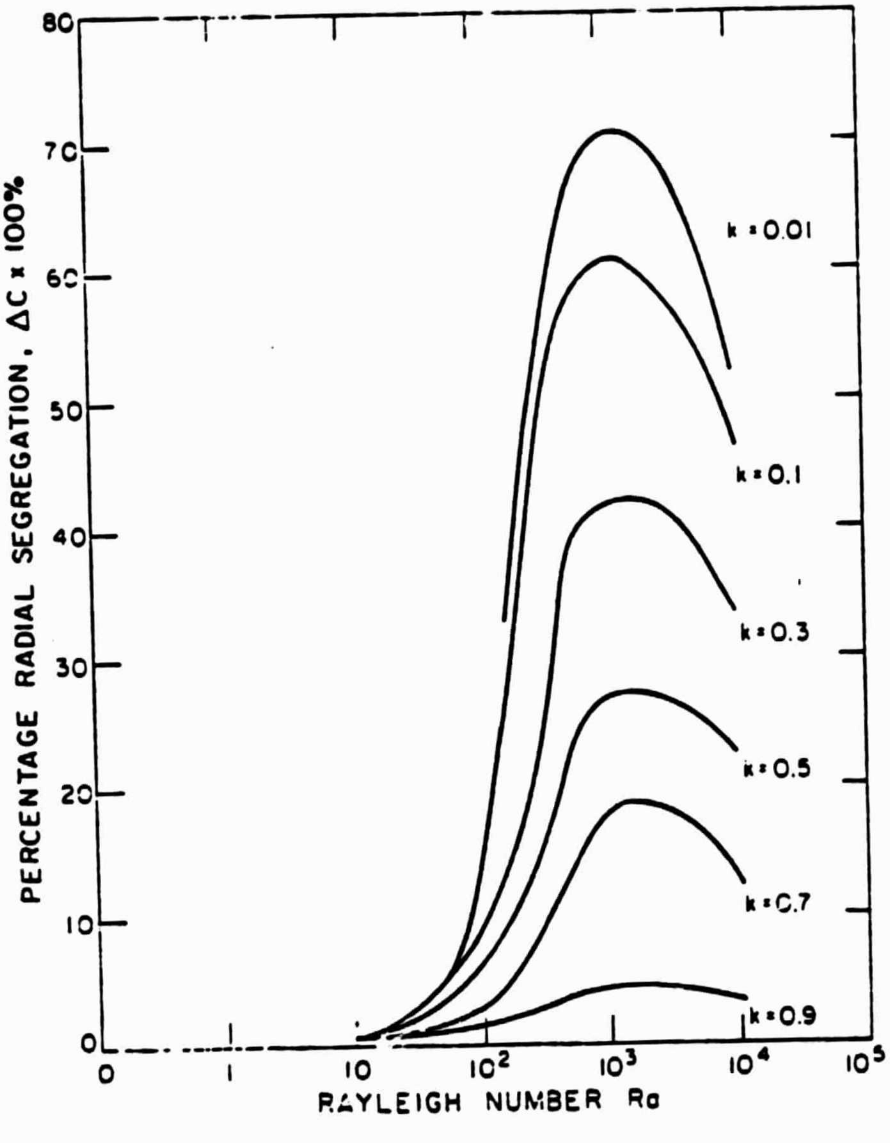

Figure 10

Chang and Brown

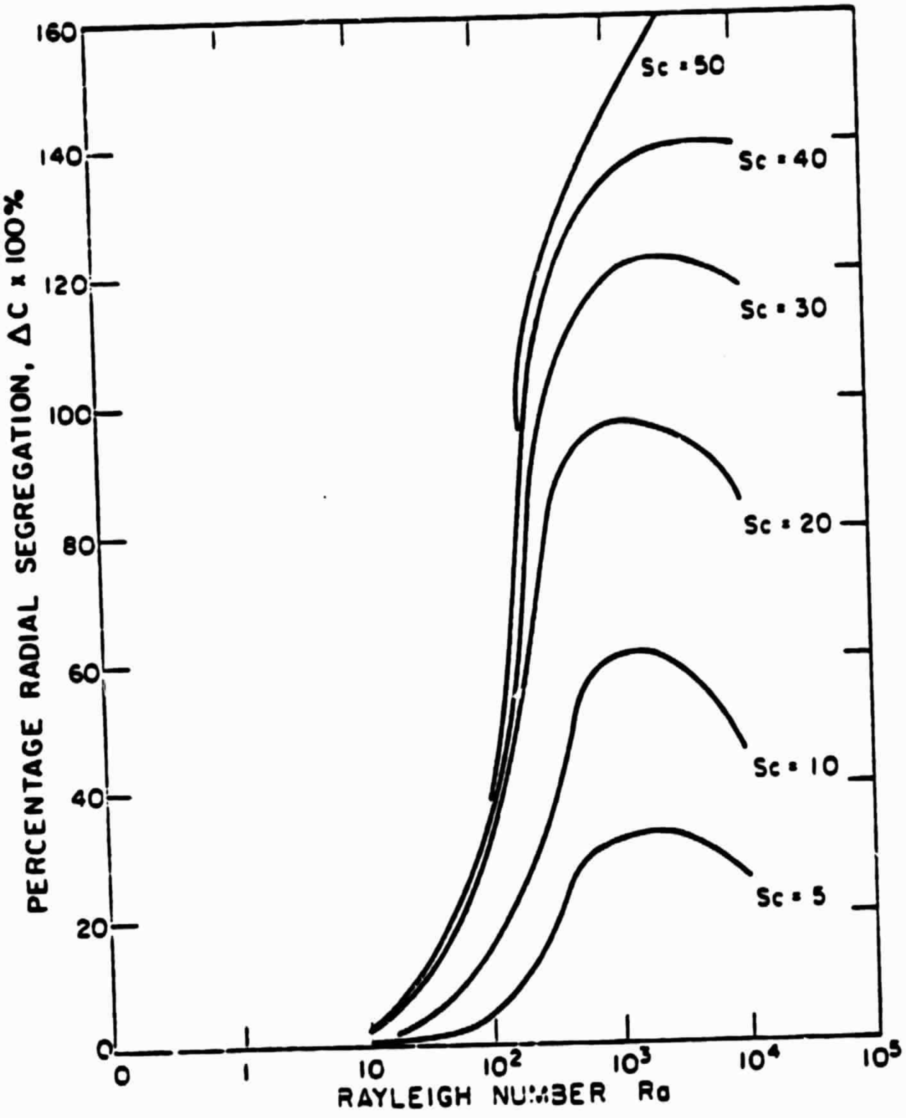

Figure 11

Chang and Brown

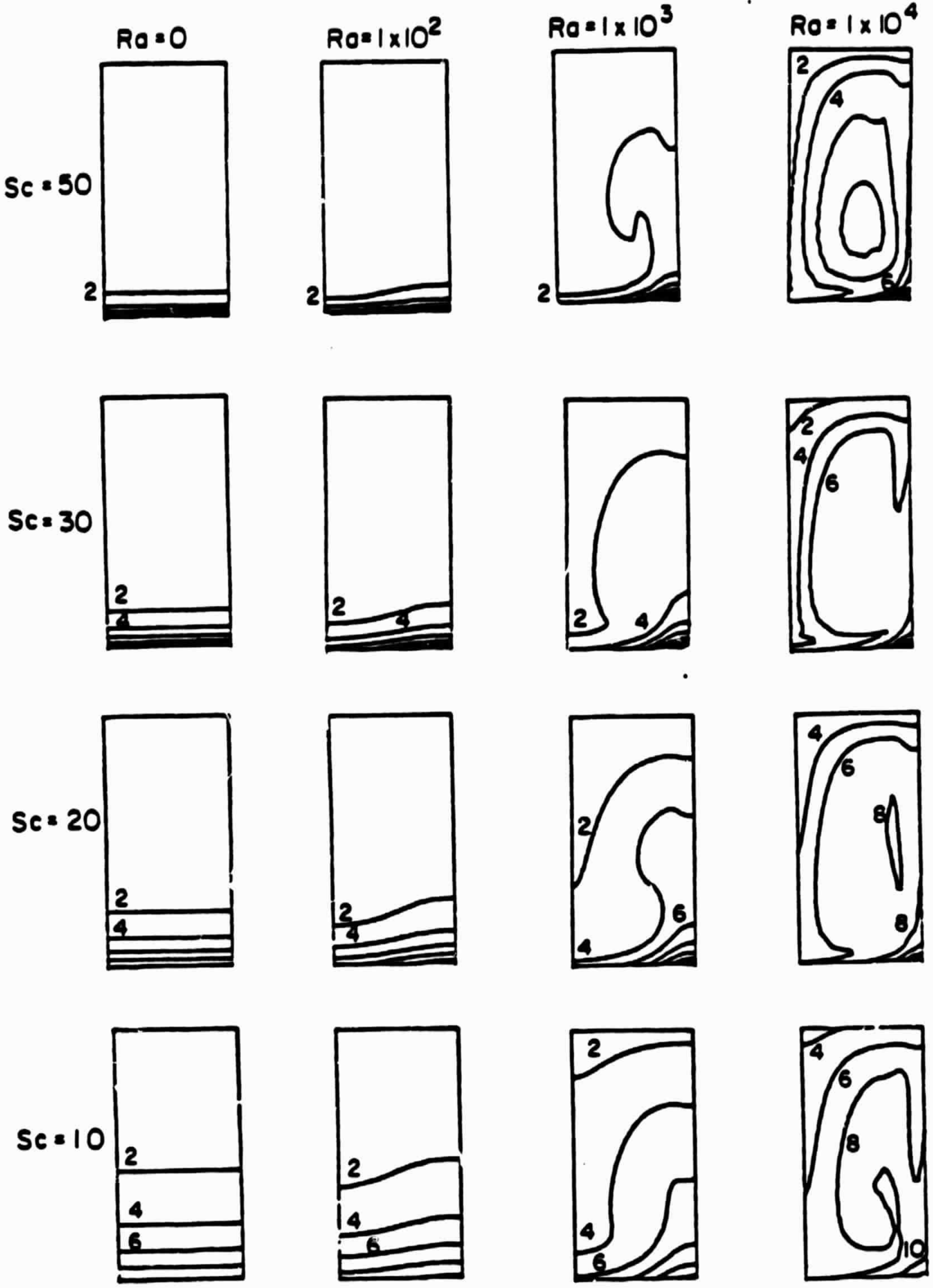

Figure 12
Chang and Brown

ORIGINAL PAGE IS
OF POOR QUALITY

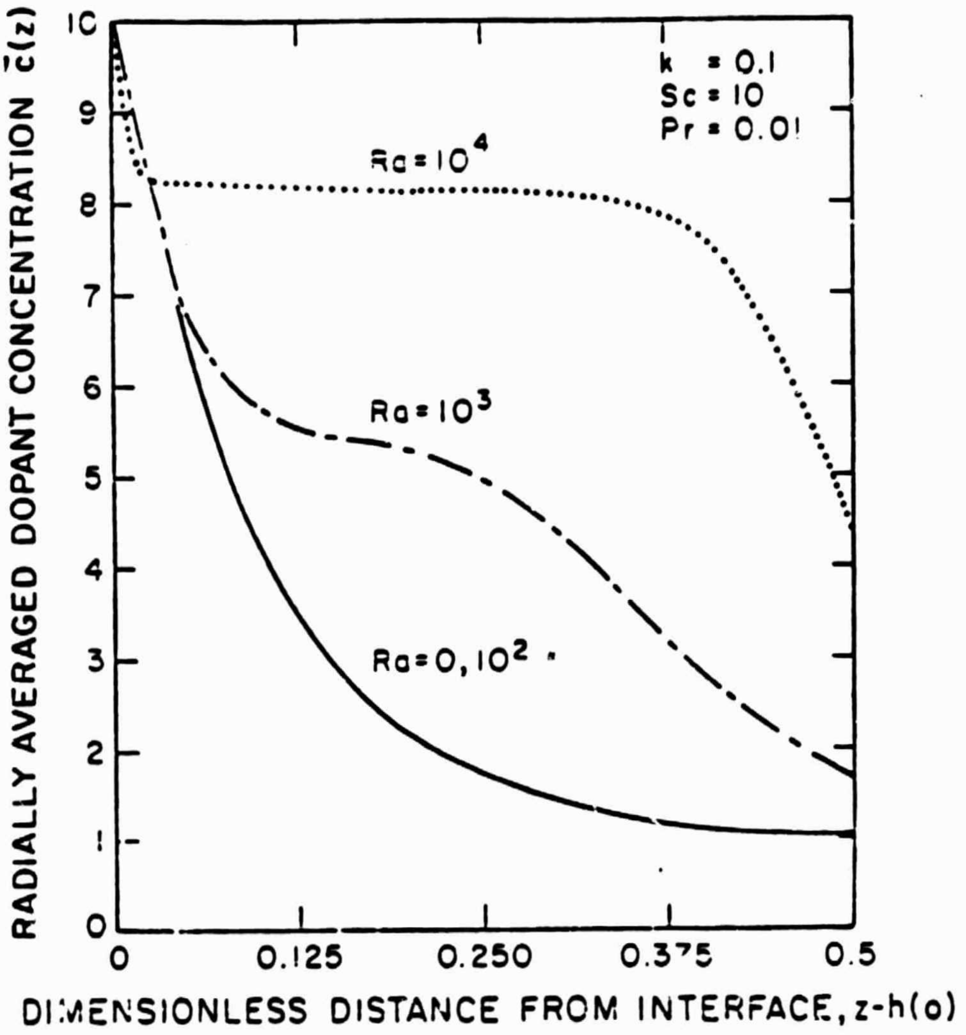

Figure 13

Chang and Brown

ORIGINAL PAGE IS
OF POOR QUALITY

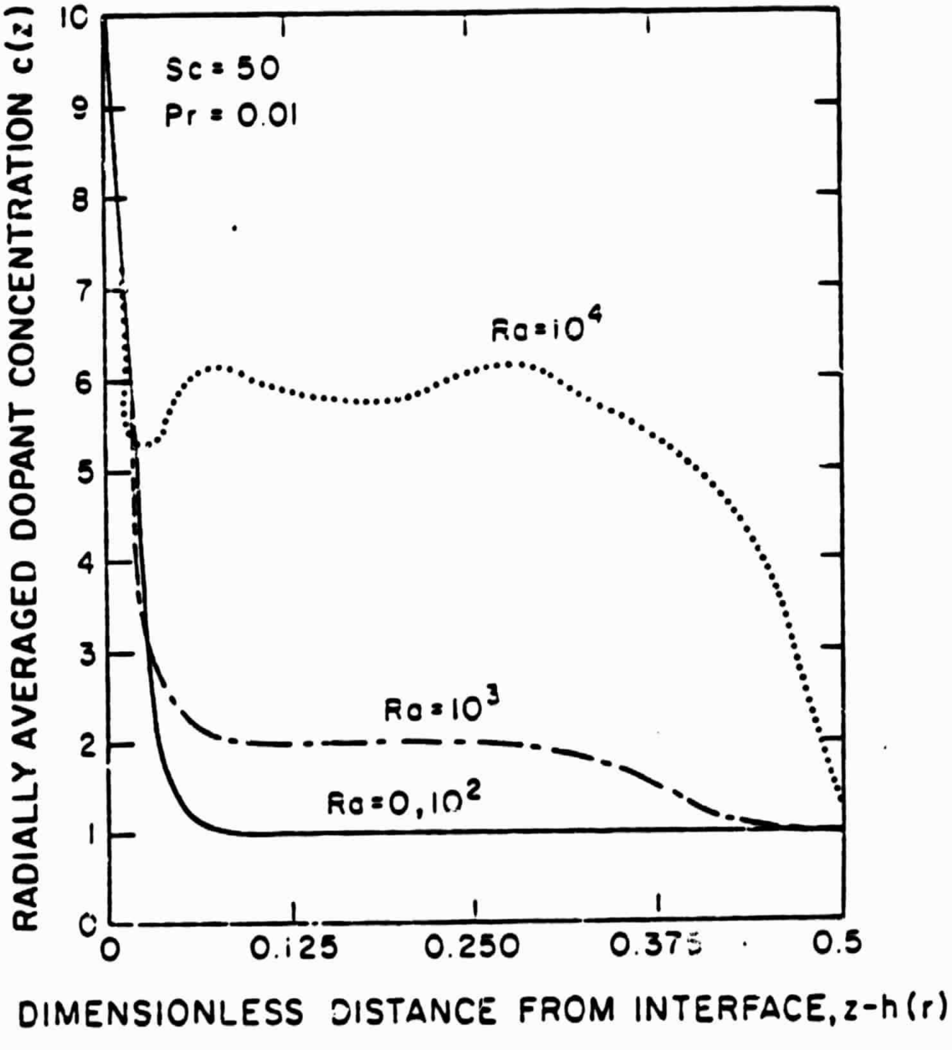

Figure 14
Chang and Brown

ORIGINAL PAGE IS
OF POOR QUALITY

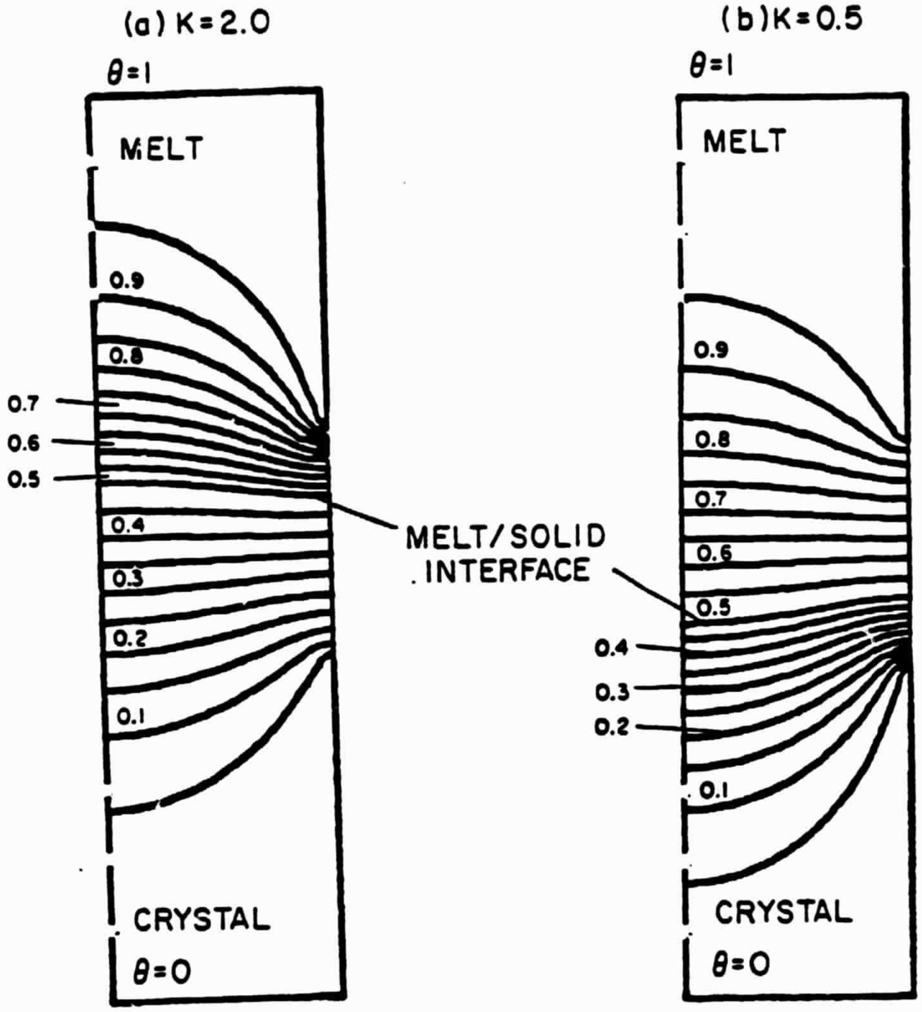

Figure 15

Chang and Brown

ORIGINAL PAGE IS
OF POOR QUALITY

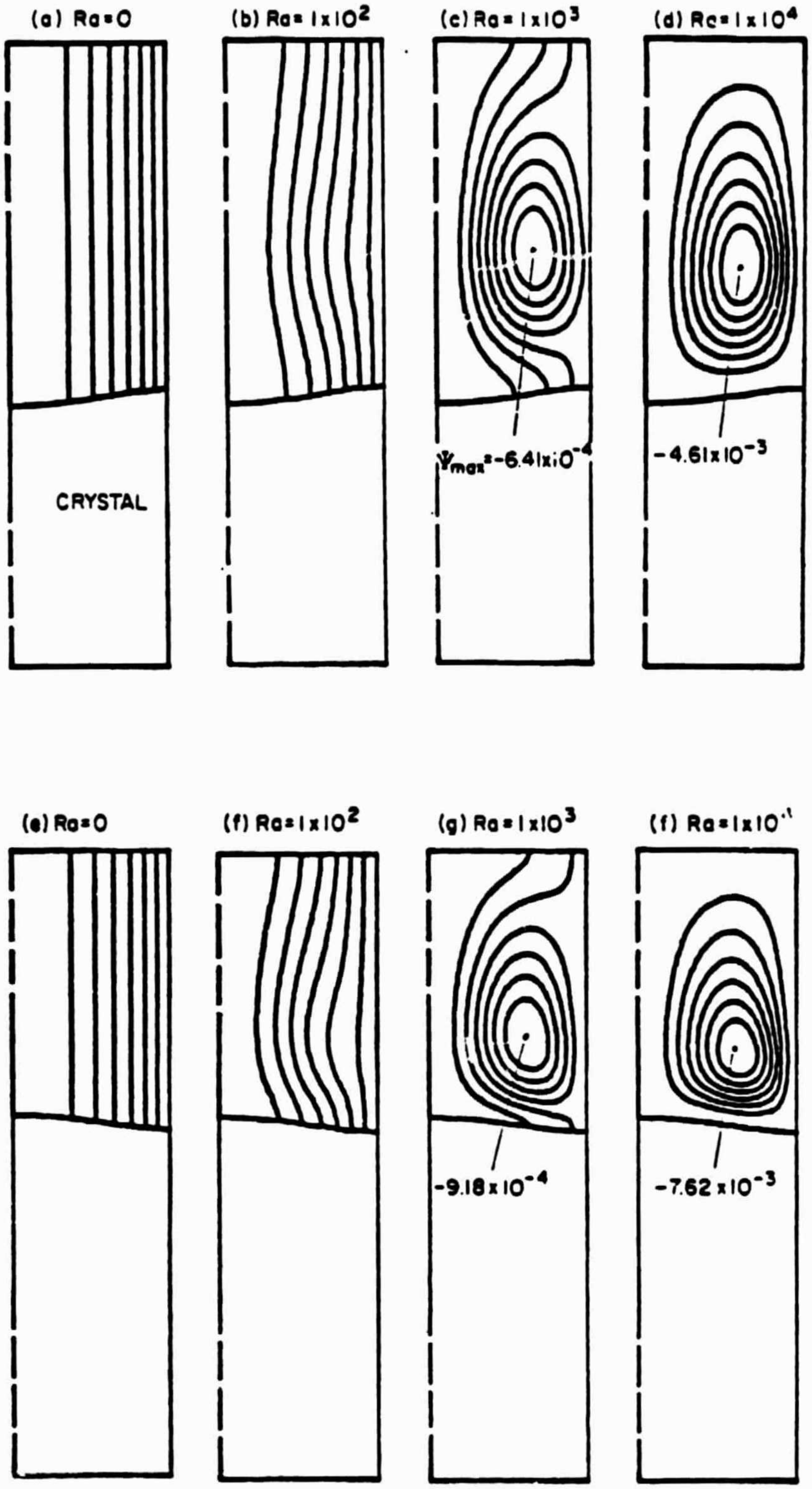

Figure 16
Chang and Brown

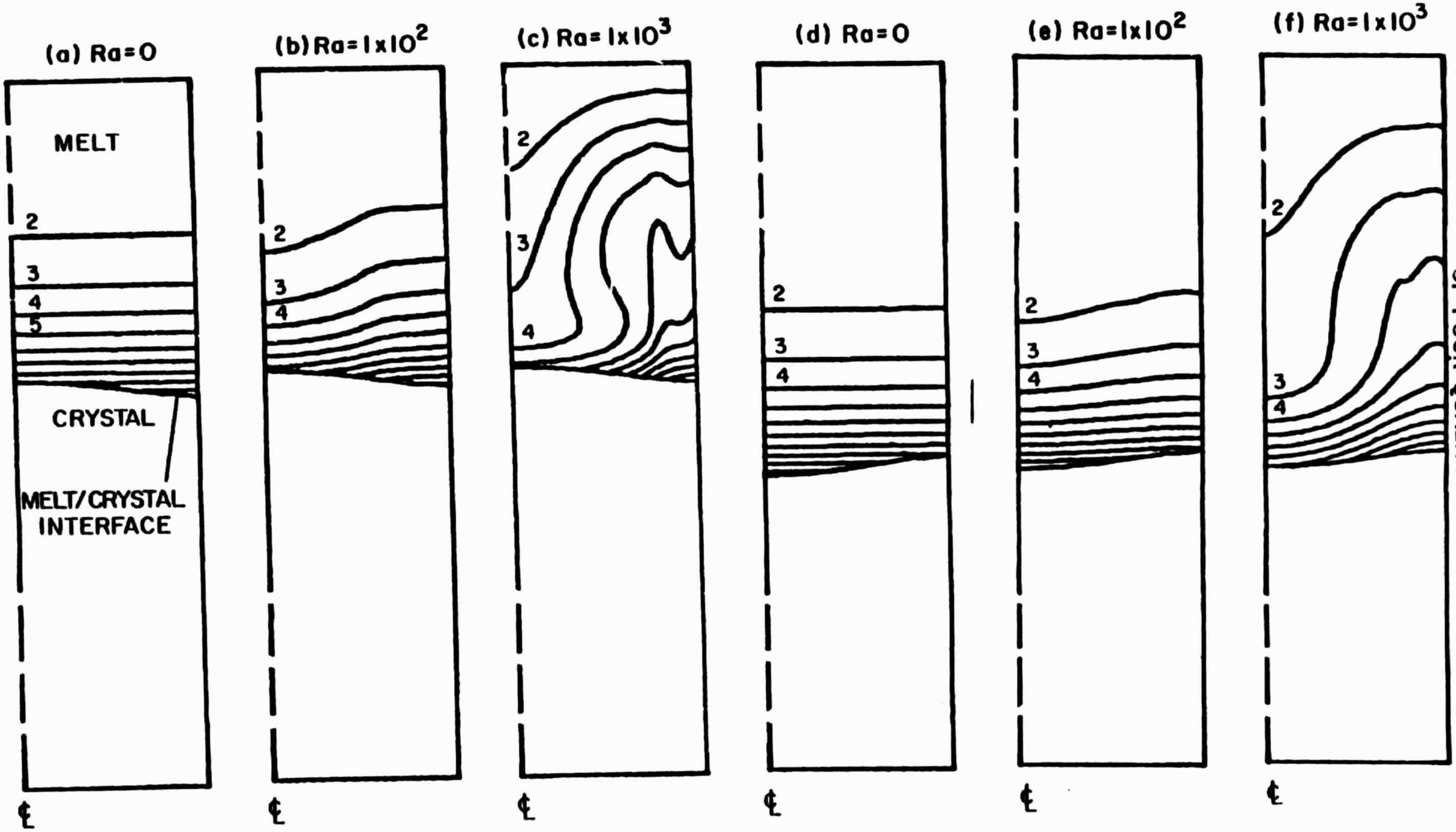

Figure 17
Chang and Brown

ORIGINAL PAGE IS
OF POOR QUALITY

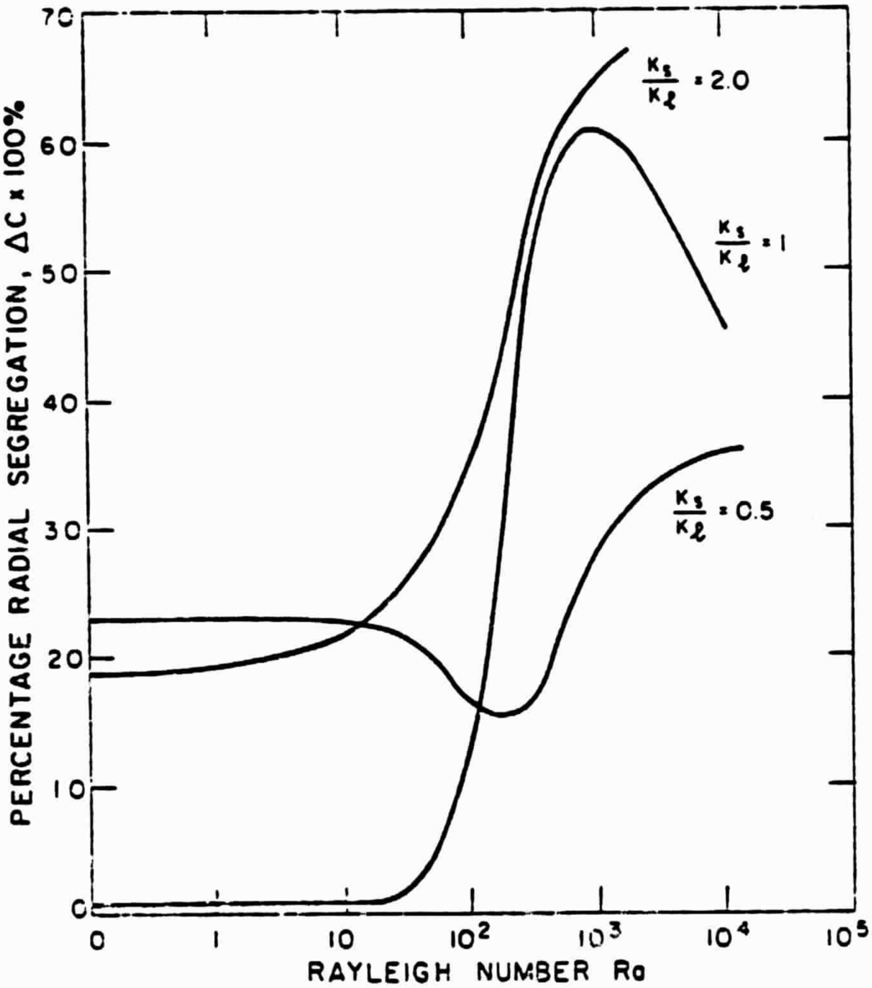

Figure 18
Chang and Brown

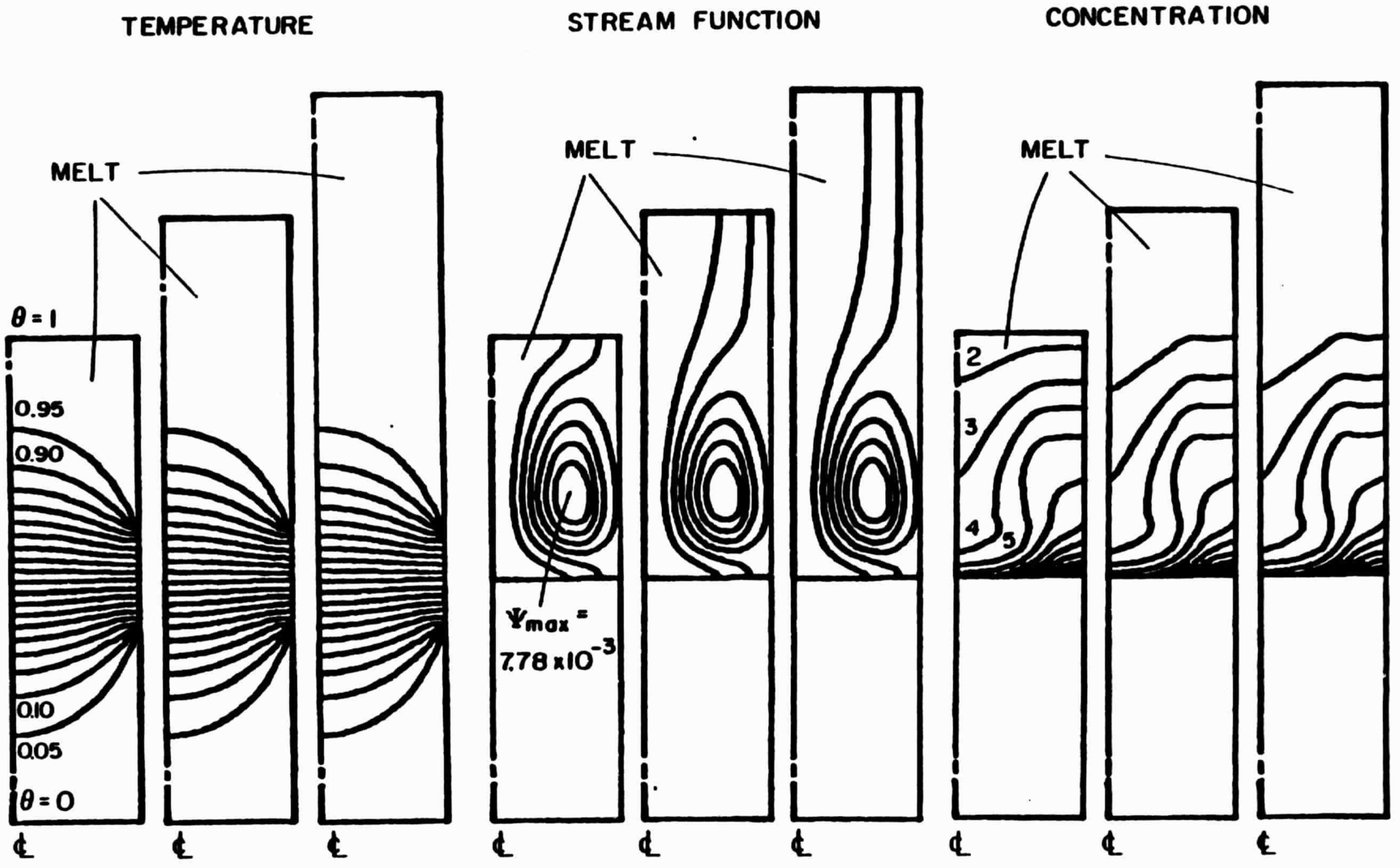

Figure 19
Chang and Brown

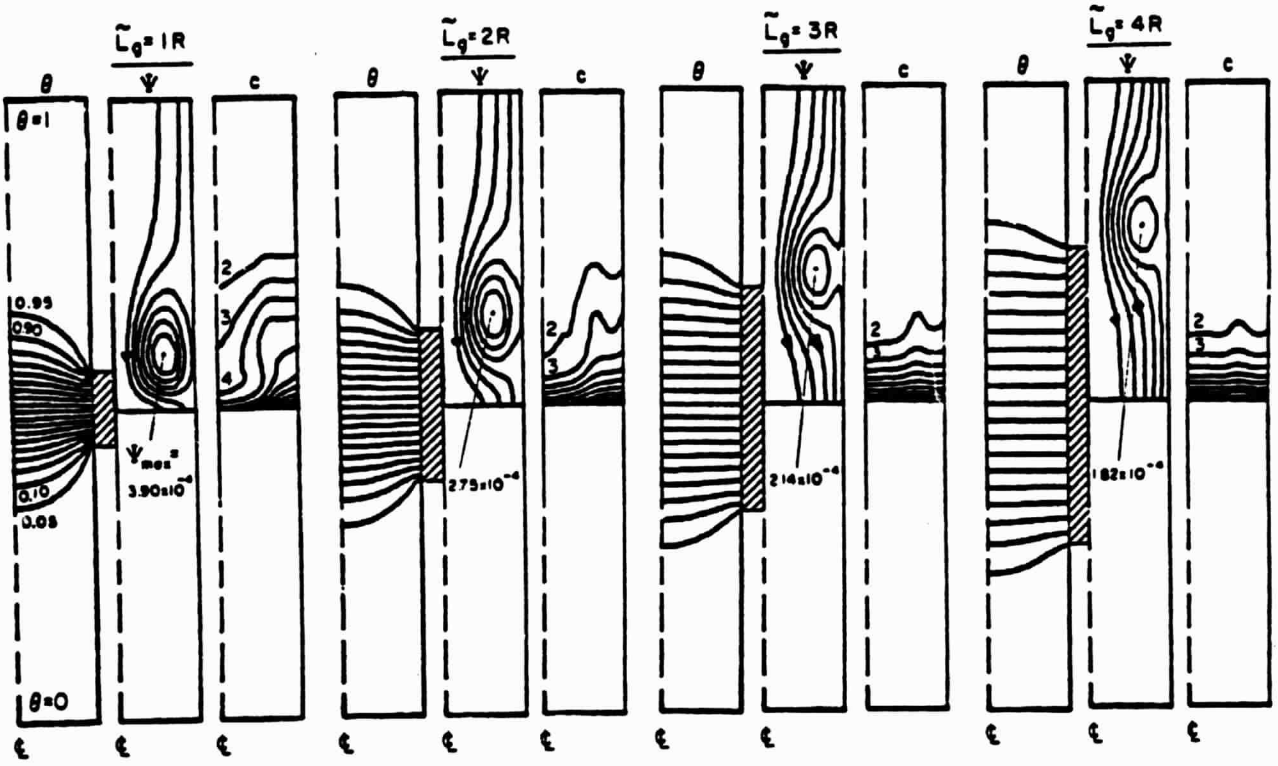

Figure 2D

Chang and Brown

ORIGINAL PAGE IS
OF POOR QUALITY

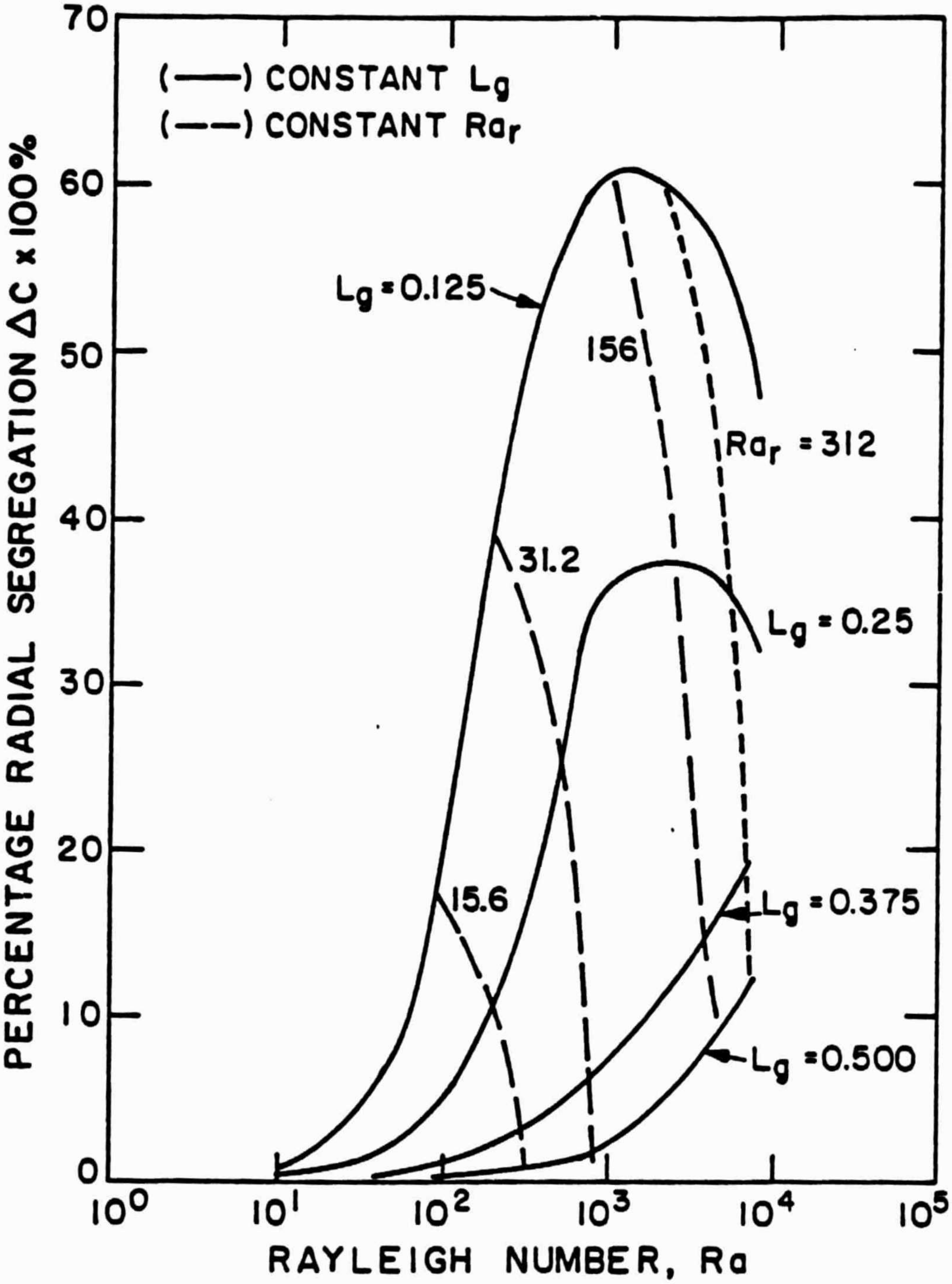

Figure 21

Chang and Bro

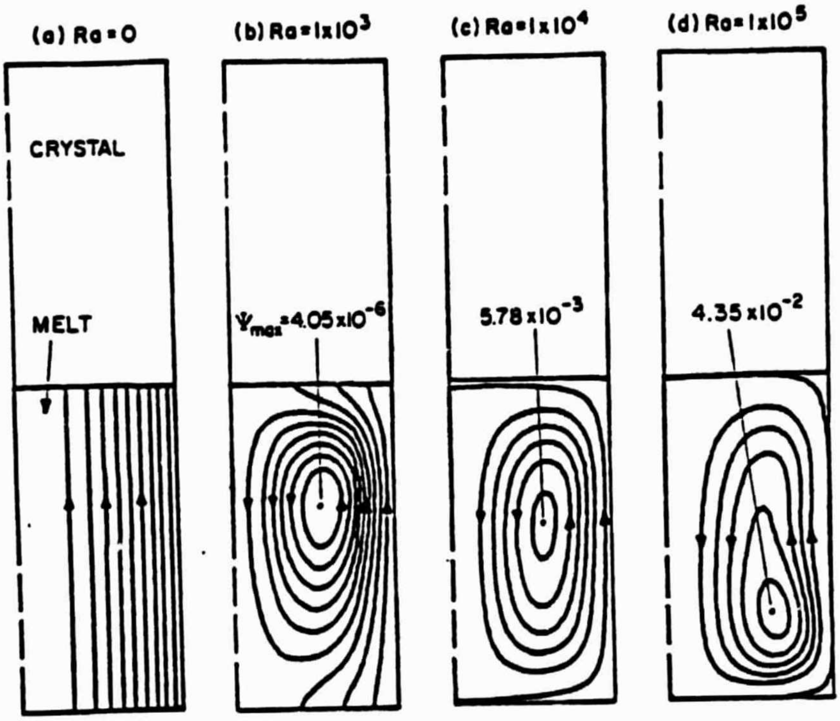

Figure 22

Chang and Brown

ORIGINAL PAGE IS
OF POOR QUALITY

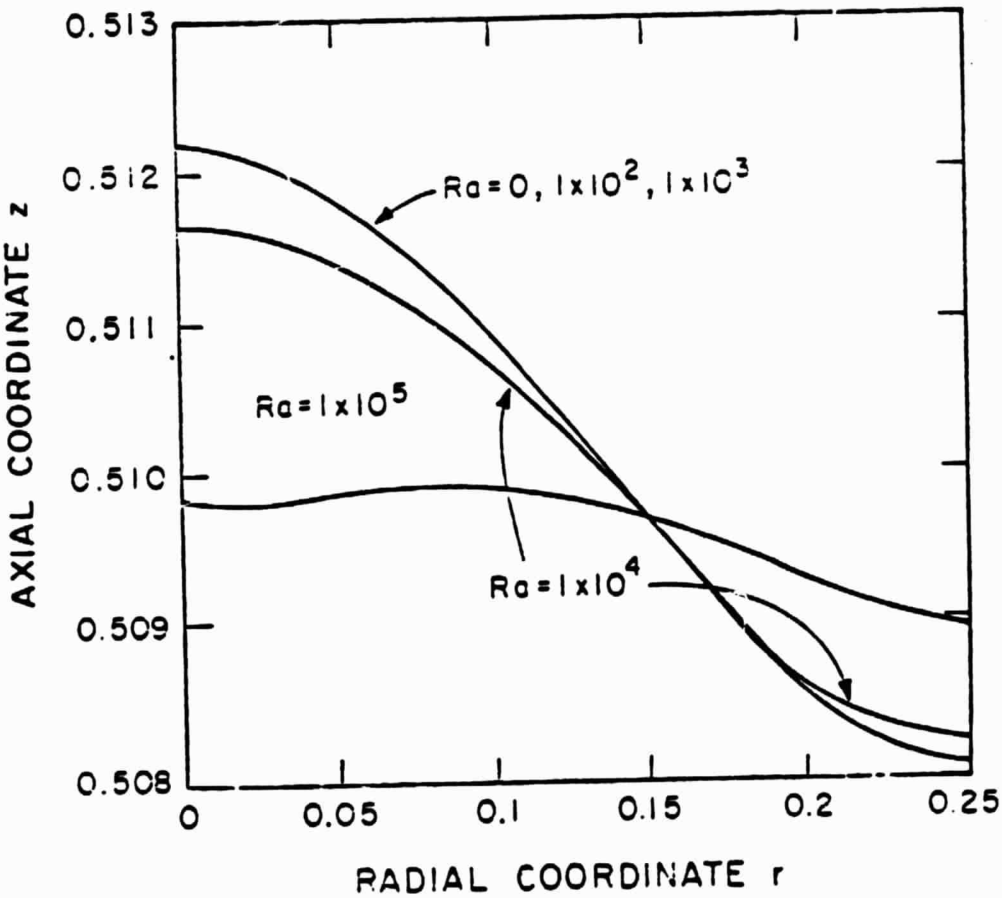

Figure 23
Chang and Brown

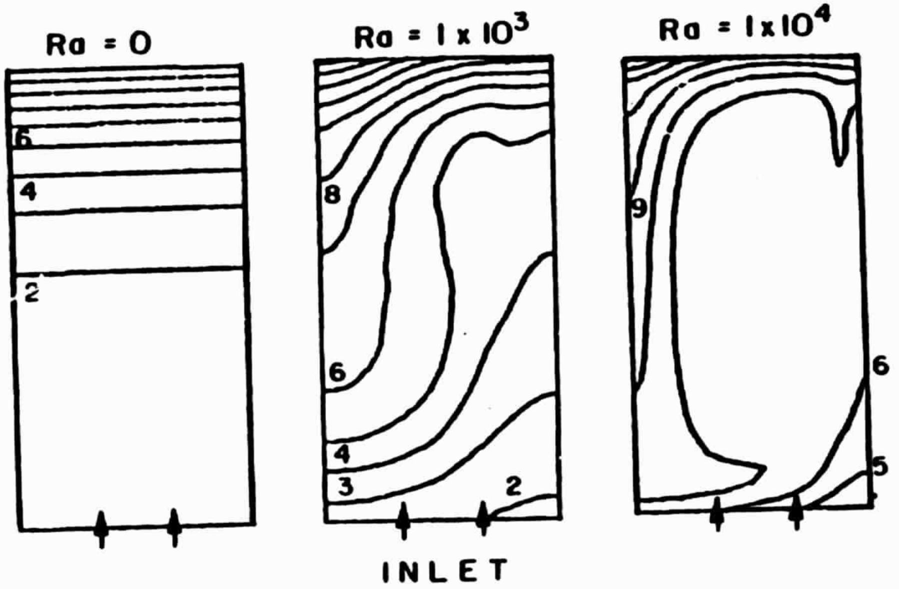

Figure 24
Chang and Brown

ORIGINAL PAGE IS
OF POOR QUALITY

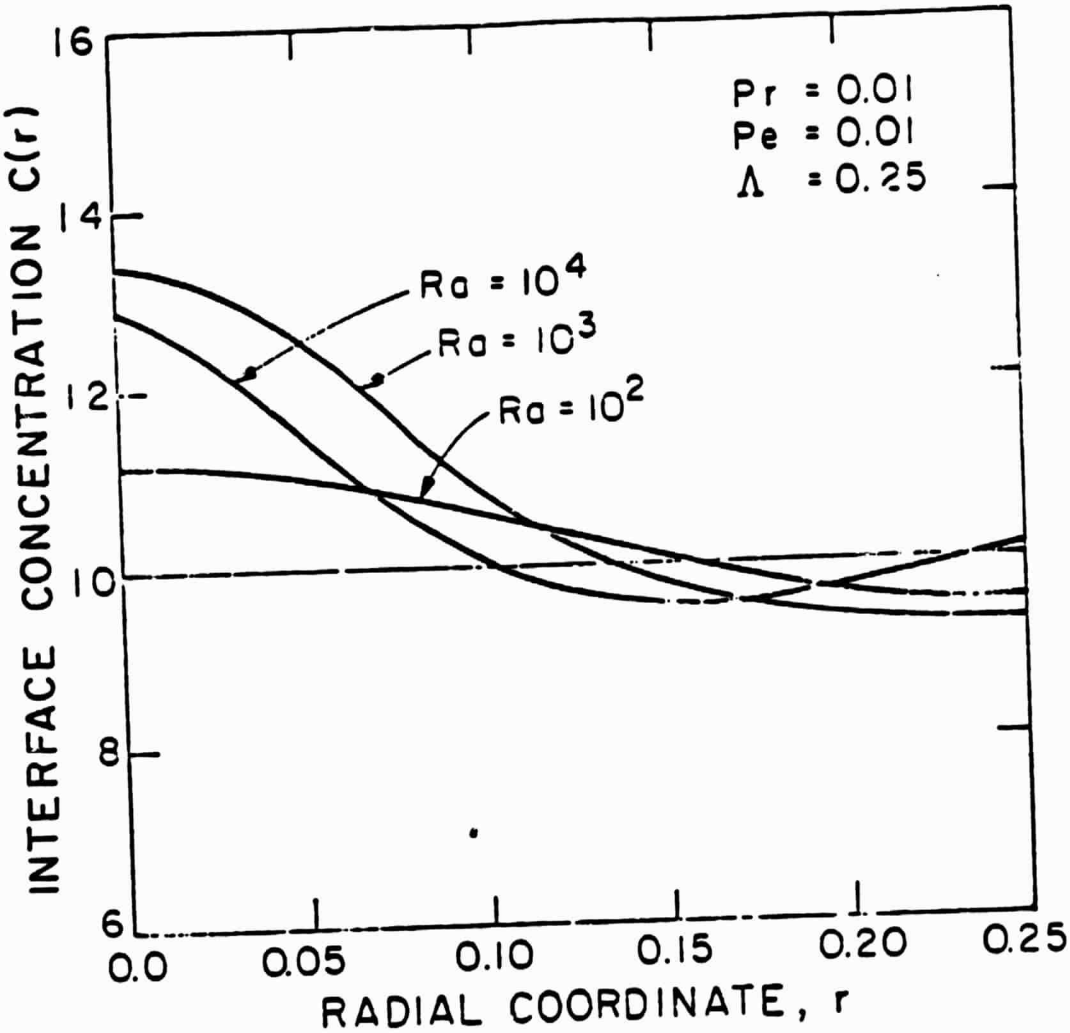

Figure 25
Chang and Br

ORIGINAL PAGE IS
OF POOR QUALITY

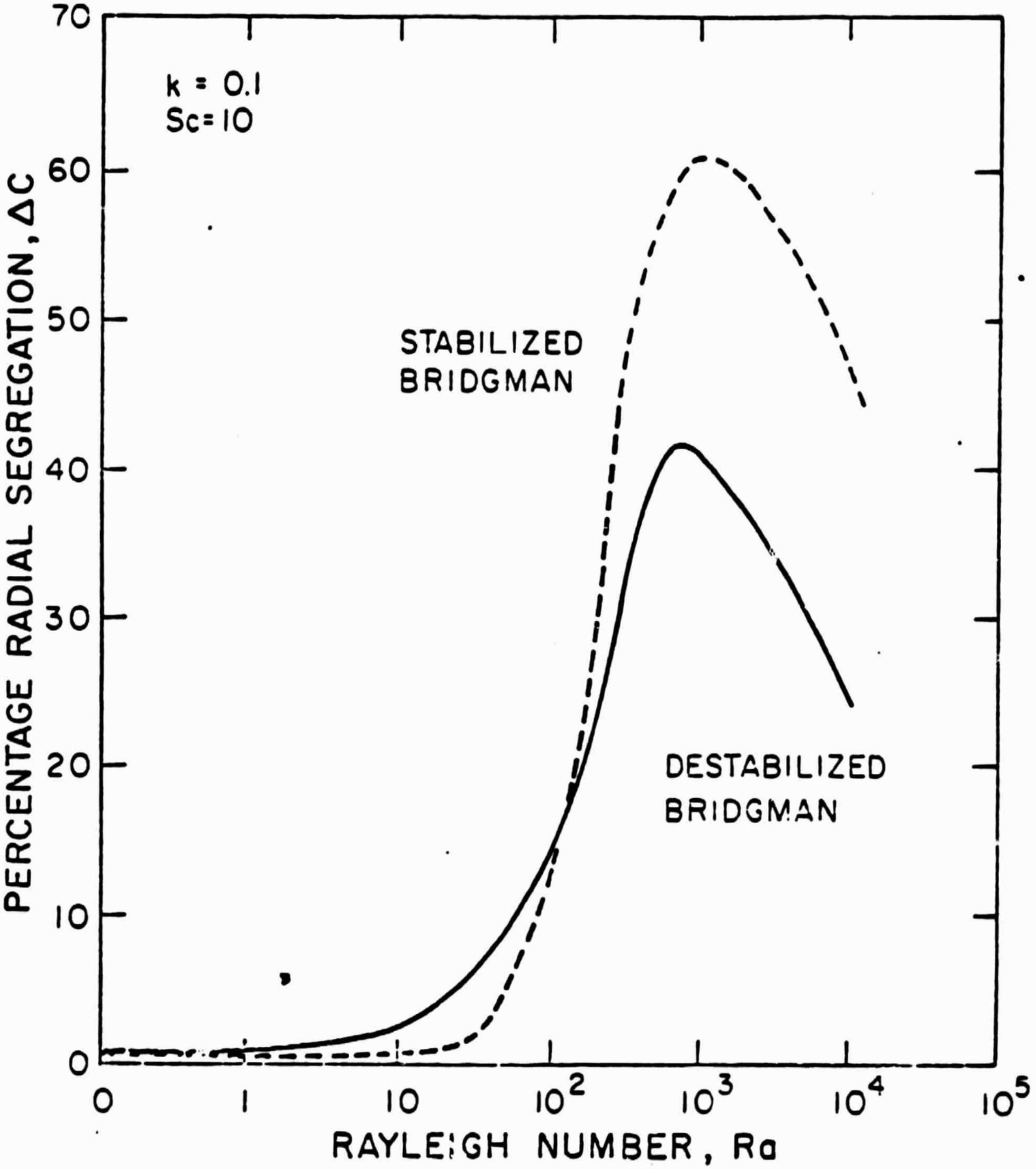

Chang and Brown
Figure 26